

# MultiDark simulations: the story of dark matter halo concentrations and density profiles.

Anatoly Klypin<sup>1\*</sup>, Gustavo Yepes<sup>2</sup>, Stefan Gottlöber<sup>3</sup>, Francisco Prada<sup>4,5,6</sup>,  
and Steffen Heß<sup>3</sup>

<sup>1</sup> *Astronomy Department, New Mexico State University, Las Cruces, NM, USA*

<sup>2</sup> *Departamento de Física Teórica M8, Universidad Autónoma de Madrid (UAM), Cantoblanco, E-28049, Madrid, Spain*

<sup>3</sup> *Leibniz-Institut für Astrophysik Potsdam (AIP), Potsdam, Germany*

<sup>4</sup> *Instituto de Física Teórica, (UAM/CSIC), Universidad Autónoma de Madrid, Cantoblanco, E-28049 Madrid, Spain*

<sup>5</sup> *Campus of International Excellence UAM+CSIC, Cantoblanco, E-28049 Madrid, Spain*

<sup>6</sup> *Instituto de Astrofísica de Andalucía (CSIC), Glorieta de la Astronomía, E-18080 Granada, Spain*

31 January 2019

## ABSTRACT

Accurately predicting structural properties of dark matter halos is one of the fundamental goals of modern cosmology. We use the new suite of MultiDark cosmological simulations to study the evolution of dark matter halo density profiles, concentrations, and velocity anisotropies. The MultiDark simulations cover a large range of masses  $10^{10} - 10^{15} M_{\odot}$  and volumes ranging from  $\sim 0.05 \text{ Gpc}^3$  to  $\sim 50 \text{ Gpc}^3$ . The total number of dark matter halos in all the simulations and redshifts exceeds 60 billion. We find that in order to understand the structure of dark matter halos and to make 1–2% accurate predictions for density profiles, one needs to realize that halo concentration is more complex than the traditionally accepted ratio of the virial radius to the core radius as in the Navarro-Frenk-White (NFW) profile. For massive halos the average density profile is far from the NFW shape and the concentration is defined by both the core radius and the shape parameter  $\alpha$  in the Einasto approximation. Combining results from different redshifts, masses and cosmologies, we show that halos progress through three stages of evolution. They start as rare density peaks that experience very fast and nearly radial infall. This radial infall brings mass closer to the center, producing a highly concentrated halo. At this stage the halo concentration increases with increasing halo mass and the concentration is defined by the  $\alpha$  parameter with a nearly constant core radius. Later halos slide into the plateau regime where the accretion becomes less radial, but frequent mergers still affect even the central region. At this stage the concentration does not depend on halo mass. Once the rate of accretion and merging slows down, halos move into the domain of declining concentration-mass relation because new accretion piles up mass close to the virial radius while the core radius is staying constant. Accurate analytical fits to the numerical results for halo density profiles and concentrations are also provided.

**Key words:** cosmology: Large scale structure - dark matter - galaxies: halos - methods: numerical

## 1 INTRODUCTION

The new and upcoming galaxy surveys will be able to measure positions of millions of galaxies. These large projects will offer good statistics and will therefore bring the opportunity to test cosmological models with high accuracy. To

keep up with the increasing precision of galaxy surveys great care has to be taken when comparing these observations with cosmological simulations. To begin with, the surveyed volumes have to be of the same size in observations and simulations. Therefore, on the one hand one needs to simulate large volumes (as in Teyssier et al. 2009; Kim et al. 2009; Crocce et al. 2010; Klypin et al. 2011; Prada et al. 2012; Alimi et al. 2012; Angulo et al. 2012; Watson et al. 2013)

\* E-mail: aklypin@nmsu.edu

and on the other hand one wants to keep the resolution high enough to retain reliable information about the properties of the halos of interest. The requirement for mass-resolution stems from the need to identify and resolve halos which can host galaxies of the observed size to be able to correctly account for galaxy bias and investigate galaxy clustering (e.g. Nuza et al. 2013).

One of the most basic and important characteristics of halos is their concentration. Without it we cannot make a prediction of the distribution of dark matter inside halos. Halo concentration – its dependence on mass, redshift, and cosmological parameters – has been the subject of extensive analysis for a long period of time (Navarro et al. 1997; Jing 2000; Bullock et al. 2001; Neto et al. 2007; Gao et al. 2008; Macciò et al. 2008; Klypin et al. 2011; Prada et al. 2012; Dutton & Macciò 2014).

Already Jing (2000) and Bullock et al. (2001) found that halo concentration  $C$  declines with mass. A simple model in Bullock et al. (2001) gave an explanation for this trend. At late stages of accretion the infalling mass stays preferentially in the outer halo regions and does not affect much the density in the center. As the result, the core radius does not change while virial radius increases with time, which results in growth of concentration with redshift  $C \propto (1+z)^{-1}$  and weak decline with halo mass  $C \propto M^{-0.1}$ .

The situation is different at early stages of halo growth when fast accretion and frequent mergers affect all parts of the halo including the central region. This results in the growth of both the virial radius and the core, which in turn leads to a constant concentration (Zhao et al. 2003, 2009). We will refer to this regime as the plateau of the concentration – mass relation.

Recently, Klypin et al. (2011) and Prada et al. (2012) discussed yet another regime for the halo concentrations: a possible increase of the concentration for the most massive halos. However, the situation with the upturn is not clear. Ludlow et al. (2012) argue that the upturn is an artifact of halos that are out of equilibrium. Dutton & Macciò (2014) did not find the upturn when they fit the Einasto profile to dark matter density profiles. They suggest that the upturn may be related with a particular algorithm of finding concentration used by Prada et al. (2012).

One of our goals for this paper is to clarify the situation with the three regimes of the halo concentration. Are the upturn halos out of equilibrium? Is the upturn an artifact or is it real?

Another complication is related with the choice of analytical approximations for the halo dark matter density profiles. It is known that the Einasto profile is more accurate than the NFW, but it has an extra parameter, which somewhat complicates the fitting procedures of density profiles. It is traditional in the field to provide fitting parameters for both Einasto and NFW approximations (e.g. Gao et al. 2008; Dutton & Macciò 2014). This produces some confusion. For example, Dutton & Macciò (2014) compare estimates of concentrations using three different methods: fitting Einasto and NFW profiles and the method used by Prada et al. (2012) (the ratio of the virial velocity to the maximum of the circular velocity). They report some disagreements between the three methods. We will revisit the issue in the paper. We will demonstrate that there is no disagreement between the methods. They simply have dif-

ferent meanings and apply to different regimes and different quantities.

In Section 2 we introduce our suite of Multidark simulation and discuss halo identification. Relaxed and unrelaxed halos are discussed in Section 3. Methods of measuring halo concentrations are presented in Section 4. The evolution of halo properties are discussed in Section 5. Results for halo concentrations are presented in Section 6. In Section 7 we discuss the halo upturn. Comparison with other published results is presented in Section 8. Possible ways of using our results to predict density profiles and concentrations are introduced in Section 9. Summary of our results is presented in Section 10. Appendix gives parameters of approximations used in our paper.

## 2 SIMULATIONS AND HALO IDENTIFICATION

Table 1 provides the parameters of our suite of simulations. Most of the simulations have  $3840^3$  particles. With simulation box sizes ranging from  $250h^{-1}\text{Mpc}$  to  $2500h^{-1}\text{Mpc}$  we have the mass resolutions of  $\sim 10^8 - 10^{10}h^{-1}M_\odot$ . Even the moderate resolution in the  $2500h^{-1}\text{Mpc}$  simulations allows us to resolve a large number of halos and subhalos that potentially host Milky way like galaxies with around  $\gtrsim 250$  particles. While this resolution does not provide reliable information about the innermost kpc of a halo, it is sufficient to estimate key properties such as halo mass, virial radius and maximum circular velocity and density profiles.

Since the uncertainties of the most likely cosmological parameters in the newest CMB Planck measurements are so small, it requires special care to be able to distinguish even small differences in the matter and halo distribution. Scaling simulations to other cosmologies, as suggested in Angulo & White (2010), is an important tool but lacks the required precision with respect to halo properties. To minimize the influence of cosmic variance (although it is small in the simulated volumes) we choose identical Gaussian fluctuations for some of our simulations. This eliminates the effect of cosmic variance when comparing the relative differences of the simulations. Initial phases were different for the MultiDark and Bolshoi simulations done with the ART code. When comparing with observations, cosmic variance needs to be considered despite the size of the surveyed volumes. This is especially necessary when studying large scales or rare objects. The initial conditions based on these fluctuations with identical initial phases for the simulation are generated with Zeldovich approximation at redshift  $z_{init} = 100$ .

The simulations we study here have been carried out with L-GADGET-2 code, a version of the publicly available cosmological code GADGET-2 (last described in Springel 2005) whose performance has been optimized for simulating large numbers of particles. We also use the Adaptive Refinement Tree (ART) code (Kravtsov et al. 1997; Gottloeber & Klypin 2008) for the MultiDark and Bolshoi simulations. This suite of simulations was analyzed with halo finding codes BDM, RockStar and FOF. Halo catalogs are provided in the public MultiDark database <sup>1</sup>.

<sup>1</sup> <http://www.multidark.org/>

**Table 1.** Numerical and cosmological parameters for the simulations. The columns give the simulation identifier, the size of the simulated box in  $h^{-1}$  Gpc, the number of particles, the mass per simulation particle  $m_p$  in units  $h^{-1} M_\odot$ , the Plummer equivalent gravitational softening length  $\epsilon$  in units of physical  $h^{-1}$  kpc, the adopted values for  $\Omega_{\text{Matter}}$ ,  $\Omega_{\text{Baryon}}$ ,  $\Omega_\Lambda$ , the clustering at  $8h^{-1}$  Mpc,  $\sigma_8$ , the spectral index  $n_s$  and the Hubble constant  $H_0$  in km/s/Mpc.

Simulation	box	particles	$m_p$	$\epsilon$	$\Omega_M$	$\Omega_B$	$\Omega_\Lambda$	$\sigma_8$	$n_s$	$H_0$	Code	Ref.
BigMD27	2.5	3840 <sup>3</sup>	$2.1 \times 10^{10}$	10.0	0.270	0.047	0.730	0.820	0.95	70.0	GADGET-2	1
BigMD29	2.5	3840 <sup>3</sup>	$2.2 \times 10^{10}$	10.0	0.289	0.047	0.711	0.820	0.95	70.0	GADGET-2	1
BigMD31	2.5	3840 <sup>3</sup>	$2.4 \times 10^{10}$	10.0	0.309	0.047	0.691	0.820	0.95	70.0	GADGET-2	1
BigMDPL	2.5	3840 <sup>3</sup>	$2.4 \times 10^{10}$	10.0	0.307	0.048	0.693	0.829	0.96	67.8	GADGET-2	1
BigMDPLnw	2.5	3840 <sup>3</sup>	$2.4 \times 10^{10}$	10.0	0.307	0.048	0.693	0.829	0.96	67.8	GADGET-2	1
MDPL	1.0	3840 <sup>3</sup>	$1.5 \times 10^9$	5	0.307	0.048	0.693	0.829	0.96	67.8	GADGET-2	1
MultiDark	1.0	2048 <sup>3</sup>	$8.7 \times 10^9$	7.0	0.270	0.047	0.730	0.820	0.95	70.0	ART	2
SMDPL	0.4	3840 <sup>3</sup>	$9.6 \times 10^7$	1.5	0.307	0.048	0.693	0.829	0.96	67.8	GADGET-2	1
BolshoiP	0.25	2048 <sup>3</sup>	$1.5 \times 10^8$	1.0	0.307	0.048	0.693	0.829	0.96	67.8	ART	1
Bolshoi	0.25	2048 <sup>3</sup>	$1.3 \times 10^8$	1.0	0.270	0.047	0.730	0.820	0.95	70.0	ART	3

1- This paper, 2- Prada et al. (2012), 3- Klypin et al. (2011)

In this paper we use results of the spherical overdensity Bound Density Maxima (BDM) halofinder (see Klypin & Holtzman 1997; Riebe et al. 2013). The BDM halo finder was extensively tested and compared with other halofinders (Knebe et al. 2011; Behroozi et al. 2013). Among other parameters, BDM provides virial masses and radii. The virial mass is defined as mass inside the radius encompassing a given density contrast  $\Delta$ . We use two definitions: the overdensity  $\Delta = 200$  relative to the critical density of the Universe  $\rho_{\text{cr}}$ , and the so called “virial” overdensity  $\Delta_{\text{vir}}(z)$  relative to the matter density  $\rho_{\text{m}}$ , which is computed using the approximation of Bryan & Norman (1998):

$$M_{200} = \frac{4\pi}{3} 200\rho_{\text{cr}} R_{200}^3, \quad (1)$$

$$M_{\text{vir}} = \frac{4\pi}{3} \Delta_{\text{vir}}(z) \rho_{\text{m}} R_{\text{vir}}^3 \quad (2)$$

The BDM halofinder provides a number of properties for each halo. In addition to  $M_{200}$  and  $M_{\text{vir}}$  it lists the maximum value of the circular velocity  $V_{\text{max}}$ :

$$V_{\text{max}} = \sqrt{\frac{GM(< r)}{r}} \Big|_{\text{max}}. \quad (3)$$

BDM also gives the halo spin parameter  $\lambda$ , the offset parameter  $X_{\text{off}} = |\mathbf{r}_{\text{centr}} - \mathbf{r}_{\text{cm}}|/R_{\text{vir}}$  - the distance between halo position (largest potential) and the halo center of mass normalized to the virial radius, and the virial ratio  $2K/W - 1$ , where  $K$  is the total kinetic energy of internal velocities and  $W$  is the absolute value of the potential energy.

To increase the mass coverage of halo properties we combine the results of the simulations with varying box size and mass resolution. The smaller box simulations offer better numerical resolution, and hence, have a more complete set of objects with low masses. Rare massive objects are sampled with small statistics because the simulated volume is smaller.

The halo density profiles and concentrations  $C$  depend on redshift  $z$  and halo mass  $M$  in a complicated way. Instead of mass and redshift it is often more physically motivated to relate halo properties with the height  $\nu$  of the density peak in the linear density fluctuation field smoothed using the top-hat filter with mass  $M$  (e.g., Prada et al. 2012; Diemer & Kravtsov 2014a). According to a simple top-hat model of collapse, peaks that exceed density contrast

$\delta_{\text{cr}} \approx 1.68$  collapse and produce halos with mass larger than  $M$ . In reality, formation of halos is neither spherical nor simple, but the notion of the peaks in the linear density perturbation field remains very useful. It is defined as

$$\nu \equiv \frac{\delta_{\text{cr}}}{\sigma(M, z)}, \quad (4)$$

where  $\sigma(M, z)$  is the rms fluctuation of the smoothed density field:

$$\sigma^2(M) = 4\pi \int_0^\infty P(k) W^2(k, R_F) k^2 dk, \quad (5)$$

where  $P(k)$  is the linear power spectrum of perturbations and  $W(k, R_F)$  is the Fourier spectrum of the top-hat filter with radius  $R_F$  corresponding to mass  $M$ .

We start the analysis of our simulations by presenting few basic statistics: the power spectra and mass functions. We have two goals with these results: (1) show the power of very large and accurate simulations and (2) demonstrate the smooth transition of halo properties and the lack of jumps from one simulation to another.

Figure 1 shows the evolution of the power spectrum of dark matter fluctuations in BigMDPL (circles), MDPL (triangles) and BolshoiP (squares) simulations. There is a remarkably good agreement between the simulations in overlapping regions. The plot also demonstrates with nice clarity the three dynamical regimes of growth of fluctuations: linear, quasi-linear with growth rates faster than linear and stable clustering with rates slower than quasi-linear. The power spectra and bias for dark matter halos and subhalos at redshift  $z = 1$  are shown in Figure 2. By plotting the power spectrum multiplied by  $k^{1.5}$  we can see better the Baryonic Acoustic Oscillations (BAO).

The mass functions of halos at different redshifts in the Planck cosmology are shown in Figure 3. The Tinker et al. (2008) mass function provides an excellent fit to  $z = 0$  results and slightly underestimates the mass function at high redshifts. The differential mass function shows that the convergence of halo mass in the simulations is of the order of a few per cent. Compared to the suite of simulations, the prediction of Tinker et al. (2008) which was gauged at different cosmologies over-predicts the number of halos by less

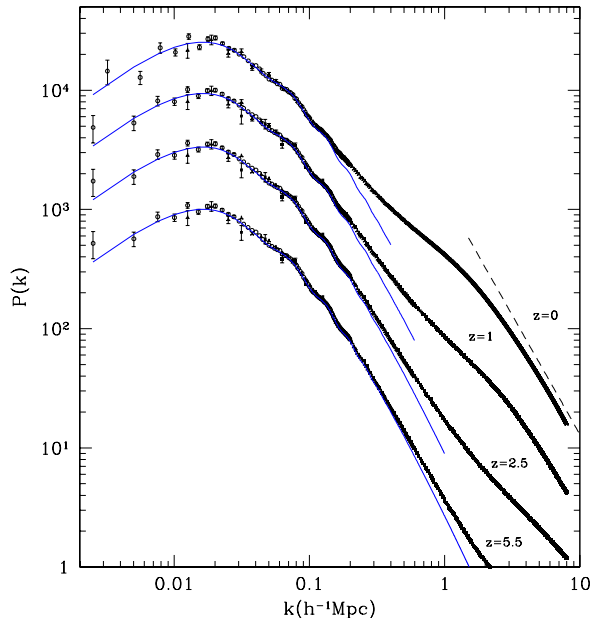


**Figure 1.** Evolution of the dark matter power spectrum in simulations with the Planck cosmological parameters for redshifts indicated in the plot. The error bars show errors assuming poissonian noise due to the finite number of independent harmonics in each bin. The full (blue) curves show the linear power spectra. Different symbols show BigMDPL (circles), MDPL (triangles), and SMDPL (squares) simulations. The plot shows that there are three regimes of growth of perturbations: (1) Linear growth of perturbations on long waves gradually shrinks as indicated by the point where the non-linear power spectrum starts to deviate upward from the linear theory prediction, (2) Mildly non-linear regime where fluctuations grow substantially faster than the linear growth, (3) Strongly non-linear regime where fluctuations start to approach relatively slow self-similar clustering, and the power spectrum is the power-law with slope  $\sim -2$  indicated by the dashed line in the plot.

than 4% for halos below  $10^{15} h^{-1} M_{\odot}$ . (For definiteness we employed a quadratic interpolation to get the parameters for  $200\Delta_{crit}$ :  $A = 0.224$ ,  $a = 1.67$ ,  $b = 1.80$ ,  $c = 1.48$ )

### 3 RELAXED HALOS

Some dark matter halos may experience significant merging or strong interactions with environment that distort their density and kinematics, and hence, may bias the estimation of halo concentrations. To avoid possible biases due to non-equilibrium effects, we select and separately study halos that are expected to be close to equilibrium. Because halos grow in mass and have satellites moving inside them, there are no truly relaxed halos. However, by applying different selection conditions, we can select halos that are less affected by recent mergers and are closer to equilibrium.

A number of diagnostics have been used to select relaxed halos. These include the virial parameter  $2K/|W| - 1$ , where  $K$  and  $W$  are the kinetic and potential energies, the offset parameter  $X_{off}$  (distance between halo center and the center of mass), and the spin parameter  $\lambda$  (e.g. Neto et al. 2007; Macciò et al. 2007, 2008; Prada et al. 2012).

In addition to these three diagnostics, Neto et al. (2007)

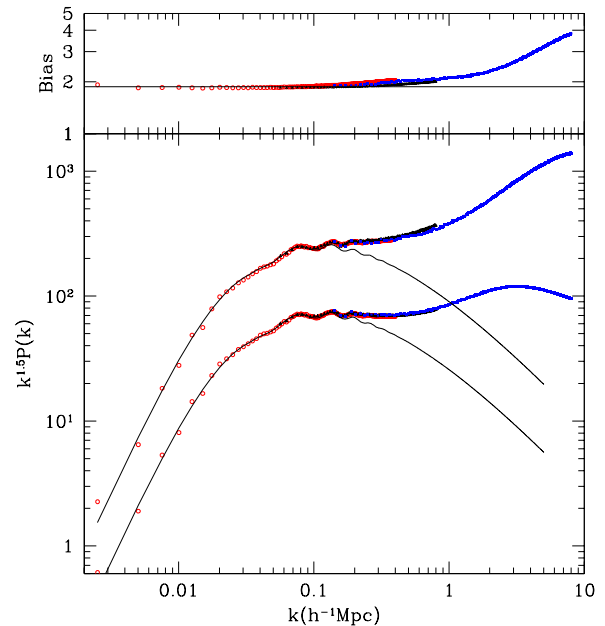


**Figure 2.** Power spectra (bottom panel) and halo bias (top panel) at redshift  $z = 1$ . Different symbols show BigMDPL (circles), MDPL (triangles), and SMDPL (squares) simulations. *Bottom panel:* Power spectra for dark matter (lower curves) and halos (top curves). The power spectra are multiplied by factor  $k^{1.5}$  to see more clearly the BAO peaks. The full curves show the linear power spectrum and the linear power spectrum scaled up with bias factor  $b = 1.95$ . Top set of symbols are for dark matter halos with circular velocities  $v_{max} > 250 \text{ km/s}$ . *Top panel:* Bias factor  $b(k) = \sqrt{P_{halos}/P_{nonlinDM}}$ .

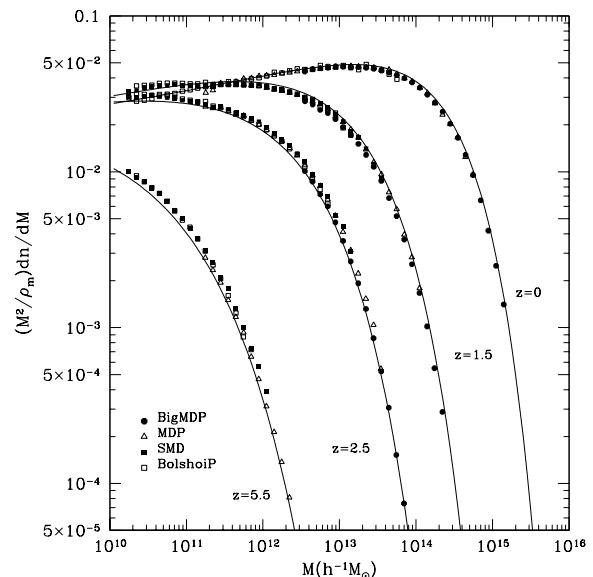


**Figure 3.** Evolution of the halo mass function in simulations with the Planck cosmological parameters. Different symbols show results from different simulations. The full curves correspond to the Tinker et al. (2008) mass function. It gives an excellent fit to  $z = 0$  results and slightly underestimates the mass function at high redshifts.

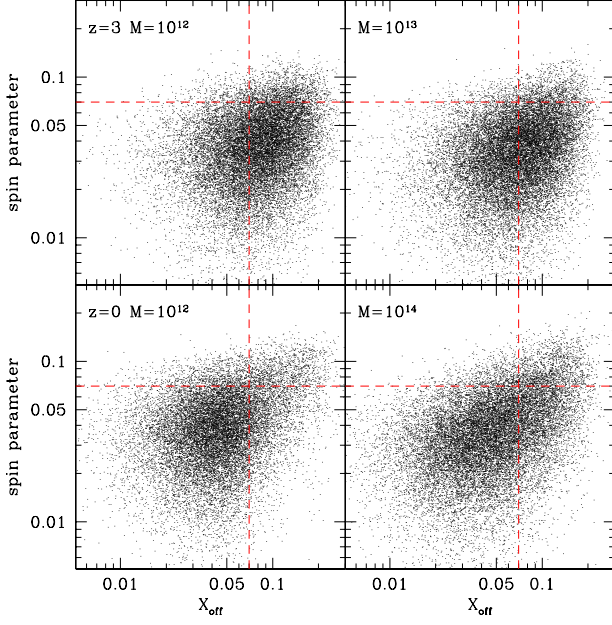


**Figure 4.** Distribution of the offset  $X_{\text{off}}$  and spin  $\lambda$  parameters for halos in the MDPL simulation at  $z = 0$  (bottom panels) and  $z = 3$  (top panels), for masses indicated in the plot. Dashed lines show the selection of relaxed halos: only halos in the low left quadrants are considered to be candidates for relaxed halos. In addition to  $\lambda$  and  $X_{\text{off}}$  we also use the virial parameter  $2K/|W| - 1$ .

and Ludlow et al. (2012, 2014) also require that the fraction of mass in subhalos  $f_{\text{sub}}$  should be small, i.e.  $f_{\text{sub}} < 0.1$ . This seems to be a reasonable condition, but we decided not to use it for two reasons. First, it is redundant: a combination of cuts in  $\lambda$  and  $X_{\text{off}}$  already remove the vast majority of cases with  $f_{\text{sub}} > 0.1$ . Figure 2 in Neto et al. (2007) clearly shows this. Second, this condition is very sensitive to resolution. Concentrations are often measured for halos with few thousand particles. For these halos one can reliably measure the spin and offset parameters, but detection of many subhalos is nearly impossible.

Figure 4 shows the distribution of spin  $\lambda$  and offset  $X_{\text{off}}$  parameters for halos in the MDPL simulation at different redshifts and different masses. Note that the distribution of spin parameters is nearly independent of mass and redshift, a well known fact. Unlike the spin parameter, the distribution of  $X_{\text{off}}$  visibly evolves with time. Dashed lines in the plot show our condition for relaxed halos:

$$X_{\text{off}} < 0.07, \text{ and } \lambda < 0.07. \quad (6)$$

Depending on redshift and mass, these conditions could select as “relaxed” most ( $\sim 80\%$  for low mass halos at  $z = 0$ ) or small ( $\sim 30\%$  for very massive halos at  $z = 3$ ) halo population.

In addition to the  $\lambda$  and  $X_{\text{off}}$  diagnostics we also use the virial parameter  $2K/|W| - 1$ . If halos are relaxed and isolated, then this parameter should be close to zero. Right panels in Figure 5 show the results for halos in the MDPL simulation at  $z = 0$  and  $z = 3$ .

As it has been known for a long time that even the

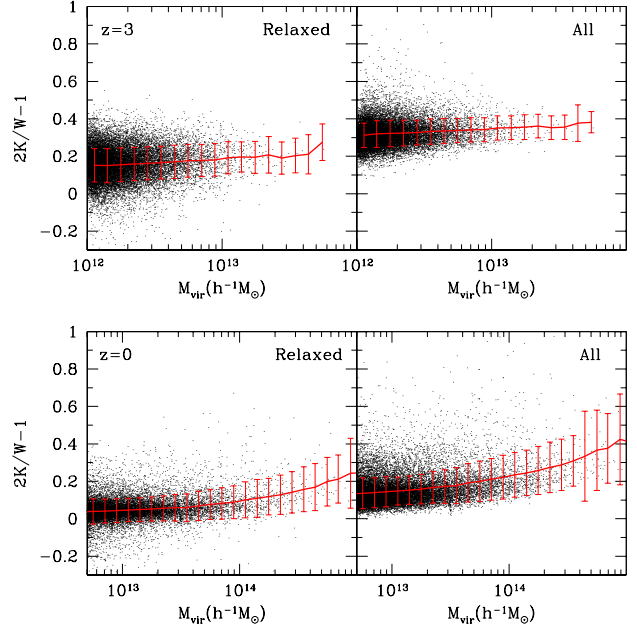


**Figure 5.** Distribution of virial parameters  $2K/|W| - 1$  for halos in the MDPL simulation at  $z = 0$  (bottom panels) and  $z = 3$  (top panels). Points show a fraction of all halos to avoid crowding. The full curves show average  $2K/|W| - 1$  values for all halos with the error bars indicating the r.m.s. deviations. Right panels show uncorrected data for all halos. Left panels show halos satisfying selection conditions given by eq.(6), which were corrected for the surface pressure effect eq.(10). Note that the correction brings halos closer to equilibrium.

average virial parameter for a population of halos is not zero (e.g., Jang-Condell & Hernquist 2001; Shaw et al. 2006; Neto et al. 2007). Results show that the kinetic energy is too large for halos to be in equilibrium. However, the conclusion that even at  $z = 0$  most of halos are *significantly* out of equilibrium is not correct. This is related with too simplistic application of the virial relation. Because halos are not isolated, a number of corrections must be taken into account to assess how far from the equilibrium they really are (Shaw et al. 2006; Knebe & Power 2008; Davis et al. 2011; Power et al. 2012). Here we follow Davis et al. (2011), who presented the virial relation including effects of the surface pressure and external force. For a given halo with mass  $M_{\text{vir}}$ , radius  $R_{\text{vir}}$ , and kinetic energy  $K$ , the virial equation should be written in the following form:

$$2K + W + W_{\text{ext}} - S_p = 0, \quad (7)$$

where the contribution of the external forces to the potential energy  $W_{\text{ext}}$  and the surface pressure term  $S_p$  are:

$$W_{\text{ext}} = - \int_V \rho \mathbf{x} \frac{\partial \Phi_{\text{ext}}}{\partial x} dV, \quad (8)$$

$$S_p = \oint \rho \mathbf{x} \cdot \mathbf{v} \mathbf{v} \cdot d\mathbf{S} = \quad (9)$$

$$= 4\pi R_{\text{vir}}^3 \rho_{\text{vir}} v_r^2. \quad (10)$$

Here the surface integral in the  $S_p$  term is taken over the surface of a sphere of virial radius  $R_{\text{vir}}$ , and  $\rho_{\text{vir}}$  and  $v_r^2$  are the density and radial velocity dispersion at  $R_{\text{vir}}$ .

We did not try to estimate the correction due to external forces, though simple estimates indicate that for low concentration halos it should be similar to  $S_p$ . In order to estimate  $S_p$  we use the halo profiles and find both the density and the radial velocity dispersion at the virial radius. We then estimate the  $S_p$  term using eq. (10) and correct the virial parameter  $2K/|W| - 1$  accordingly.

Left panels in Figure 5 show the virial parameter for relaxed halos corrected for the surface pressure term. Typical value of the correction is  $\sim 0.2$ , which is similar to those found by Shaw et al. (2006); Knebe & Power (2008) and Davis et al. (2011). Corrected values of the virial parameter are significantly closer to zero. For example, halos at  $z = 0$  with mass  $M_{\text{vir}} < 10^{14} h^{-1} M_{\odot}$  are very close to equilibrium, which is a dramatic improvement considering that all of them were considered to be out of equilibrium without the surface pressure correction. Just as Davis et al. (2011), we also find that the surface pressure correction, though an improvement, is not sufficient to bring the most massive and high- $z$  halos to equilibrium. Other corrections such as external forces and non-spherical effects are expected to bring those halos even closer to equilibrium. However, it is difficult to estimate those.

Due to the uncertainty with the estimates of the virial parameter  $2K/|W| - 1$ , one can apply somewhat loose conditions to select relaxed halos. For example, following Neto et al. (2007) and Ludlow et al. (2014), we may have used  $2K/|W| < 1.35$ . The results in the right panels of Figure 5 show that this could have been a reasonable choice for  $z = 0$  halos, but not for high redshifts. For example, at  $z = 3$ , the vast majority of  $M_{\text{vir}} > 10^{13} h^{-1} M_{\odot}$  halos would be considered “unrelaxed” in spite of the fact that they are relaxed (i.e., pass the  $2K/|W| < 1.35$  condition) once the surface pressure correction is applied.

The combination of a strict criterion for the virial parameter and the lack of correction for the surface pressure produces an unwanted side effect in results of Ludlow et al. (2012, 2014). Instead of selecting more relaxed halos, which was their intention, it results in selection of a biased sample of halos with unusually low concentrations and infall velocities.

Instead of applying the surface pressure correction and considering the fact that most of severely out-of-equilibrium halos are rejected by the offset and spin parameters, we adopt the  $2K/|W| < 1.5$  selection applied to the uncorrected virial parameters.

#### 4 DEFINING AND MEASURING HALO CONCENTRATIONS AND DENSITY PROFILES

Dark matter halo density profiles are often approximated by the NFW profile (Navarro et al. 1997):

$$\rho_{\text{NFW}}(r) = \frac{\rho_0}{x(1+x)^2}, \quad x \equiv \frac{r}{r_{-2}}. \quad (11)$$

However, halo profiles can substantially deviate from the NFW shape and are much better approximated with an Einasto profile (Einasto 1965; Navarro et al. 2004;

Gao et al. 2008; Dutton & Macciò 2014):

$$\rho_{\text{Ein}}(r) = \rho_0 \exp\left(-\frac{2}{\alpha} [x^\alpha - 1]\right), \quad x \equiv \frac{r}{r_{-2}}. \quad (12)$$

Here, the radius  $r_{-2}$  is the characteristic radius of the halo where the logarithmic slope of the density profile  $d \log(\rho)/d \log(R)$  is equal to -2. It is often perceived that the Einasto profile provides accurate fits to the data because it has more free parameters: three instead of two for NFW. This conclusion is not correct. Even if the third parameter is fixed (defined by halo mass), the Einasto profile provides a better fit to simulation results (Gao et al. 2008). Nevertheless, there is a reason why the NFW profile was used for so long and why it is still a useful approximation.

The deviations of the NFW profile from  $N$ -body results are small for halos that are not massive. For these halos the NFW and Einasto profiles are very close for a large range of radii  $r = (0.01 - 1)R_{\text{vir}}$ . This point is illustrated in Figure 6 that gives examples of the circular velocity profiles  $V_{\text{circ}}^2 = GM(< r)/r$  for NFW and Einasto profiles. It shows the profiles for halos with the same virial mass and with the same characteristic radius  $r_{-2}$ , which was in this case chosen to be  $r_{-2} = R_{\text{vir}}/15$ . To relate  $\alpha$  to  $\nu$  we use eq. (13). The Einasto profiles with small  $\alpha \approx 0.15 - 0.18$  parameters that are typical for halos with peak height  $\nu < 2$ , provide reasonable (though not perfect) approximations to the NFW with  $\lesssim 10\%$  deviations for radii in the range  $R/R_{\text{vir}} = 0.05 - 1$  (e.g., Ludlow et al. 2012). The situation is different for much more massive halos, which are larger peaks of the density field. For  $\nu > 2$ , the deviations are substantial even for radii  $R/R_{\text{vir}} = 0.1 - 0.4$  where the circular velocity corresponding to the NFW profile is  $\sim 30\%$  below the Einasto profile (see also Gao et al. 2008).

The accuracy of the NFW approximation depends on parameters such as halo mass and redshift (e.g., Navarro et al. 2004). Gao et al. (2008) and Dutton & Macciò (2014) argue that the second parameter  $\alpha$  in the Einasto profile depends only on the amplitude of perturbations  $\sigma(M)$ , where  $M$  is the halo mass. Gao et al. (2008) provide the following approximation for the dependence of  $\alpha$  on the amplitude of perturbations:

$$\alpha = 0.155 + 0.0095\nu^2. \quad (13)$$

The observed large deviations from the NFW profile for high- $\nu$  peaks pose a number of problems for the estimates of halo concentrations because the concentrations are routinely estimated using NFW fits (e.g., Neto et al. 2007; Duffy et al. 2008; Diemer & Kravtsov 2014a; Dutton & Macciò 2014). Figure 7 shows an example that highlights the problem. At  $z = 1.5$  we select  $\sim 3000$  halos with mass  $M_{200} = (1 - 1.5) \times 10^{14} h^{-1} M_{\odot}$  in the BigMDPL simulation. These halos correspond to high density peaks of  $\nu \simeq 3.6$ . We then construct the median halo density profiles for these halos and present them in Figure 7 for all and for relaxed halos. The plots demonstrate that the Einasto approximation provides remarkably accurate fits for the measured profiles with deviations less than 1% for the relaxed halos. The NFW profile is much less accurate. However, the real problem with the NFW fits is the systematic errors, not the random errors. The NFW fits systematically overpredict the halo concentration by (10–20)% for the high- $\nu$  halo density profiles shown in Figure 7. This and other systematic effects

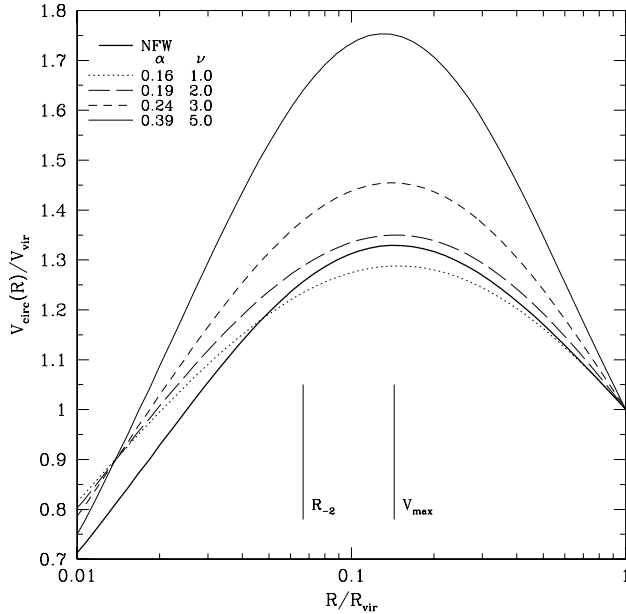


**Figure 6.** Comparison the NFW halo profile with the Einasto profiles with different parameters  $\alpha$ . Halos were fixed to have the same virial mass, and the same radius  $r_{-2}$  where the slope of the density profile is equal to  $d\log(\rho)/d\log(R) = -2$ . In cosmological simulations parameter  $\alpha$  depends of the peak height  $\nu$  with larger  $\nu$  (and, thus, larger mass  $M$ ) corresponding to larger parameters  $\alpha$ . The ratio of the maximum circular velocity to the virial velocity  $V_{\text{circ}}/V_{\text{vir}}$  is related with halo concentration for any profile.

were recently discussed by Meneghetti & Rasia (2013) and Dutton & Macciò (2014).

One may think that using the Einasto profiles to estimate concentrations would produce much better results. Unfortunately, the Einasto profile has its own critical issue when it comes to concentration. For the NFW profile the ratio  $R_{\text{vir}}/r_{-2}$  uniquely defines the density profile for given halo mass, and therefore it is a good measure for halo concentration. Yet, for the Einasto profile such a ratio is not the concentration because for the same  $R_{\text{vir}}/r_{-2}$  ratio, halos with larger  $\alpha$  are clearly denser, and thus are more concentrated. In order to understand why is that, we need to step away from the problem of fitting profiles of cosmological dark matter halos and discuss what is concentration.

The common-sense notion of concentration is that for two objects of fixed mass and radius, the object with a more dense center is more concentrated. If we consider an astronomical quasi-spherical object such as a globular cluster, an elliptical galaxy, or a dark matter halo, then a more concentrated object is the one that has denser central region and less dense outer halo. Keeping in mind this general notion of concentration, we now look again at the NFW and Einasto profiles presented in Figure 6. All the profiles in the plot have the same virial mass, virial radius and  $r_{-2}$ . However, they all have different concentrations because they have different masses inside the central  $\sim 0.1R_{\text{vir}}$  radius. This happens because the “shape parameter”  $\alpha$  in the Einasto profile affects not only the shape of the profile, but also its concentration.

Figure 8 illustrates the point. Here we analyze two Einasto profiles with the same total mass and the same ratio

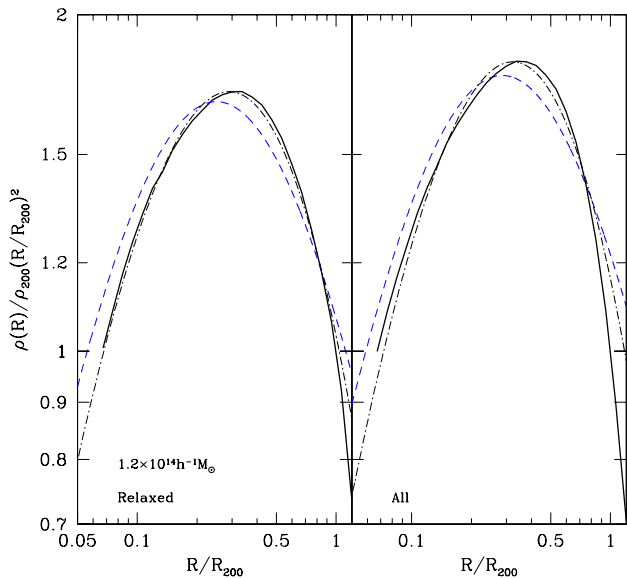


**Figure 7.** Density profiles of halos with mass  $M_{200} \approx 1.2 \times 10^{14} h^{-1} M_{\odot}$  at  $z = 1.5$  (full curves). Left (right) panels show relaxed (all) halos. Dot-dashed curves show Einasto fits, which have the same virial mass as halos in the simulation. The NFW profiles (dashed curves) do not provide good fits to the profiles and significantly depend on what part of the density profile is chosen for fits.

$R_{\text{vir}}/r_{-2} = 10$ . The only difference is the shape parameter:  $\alpha = 0.15$  and  $\alpha = 0.40$ . For these density profiles Figure 8 shows two conventional measures of concentration: radius of a given fraction of mass (bottom panel) and fraction of mass within given radius (top panel). On all accounts, the profile with larger  $\alpha$  is more concentrated. For example, the radius of  $(1/3)$  of the virial mass is about 30% smaller for the  $\alpha = 0.40$  model.

To summarize, for the Einasto profile the  $R_{\text{vir}}/r_{-2}$  ratio is not the concentration. The real concentration depends on both  $R_{\text{vir}}/r_{-2}$  and  $\alpha$ .

Following Prada et al. (2012) we use the ratio of the maximum circular velocity to the virial velocity  $V_{\text{max}}/V_{\text{vir}}$  as a *profile-independent measure of halo concentration*. The larger is the ratio, the larger is the halo concentration regardless of any particular analytical approximation of the profile.

It is convenient to write the circular velocity profile  $V_{\text{circ}}(r)$  for the NFW and Einasto approximations in the following way:

$$\left(\frac{V_{\text{circ}}(r)}{V_{\text{vir}}}\right)^2 = \frac{C_E}{x} \frac{f_E(x, \alpha)}{f_E(C_E, \alpha)} = \frac{C}{x} \frac{f(x)}{f(C)}, \quad (14)$$

$$f(x) = \ln(1+x) - \frac{x}{1+x}, \quad (15)$$

$$f_E(x, \alpha) = e^{\frac{2}{\alpha}} \int_0^x x^2 e^{-\frac{2}{\alpha} x^{\alpha}} dx, \quad (16)$$

$$x \equiv \frac{r}{r_{-2}}, \quad C = \frac{R_{\text{vir}}}{r_{-2}}. \quad (17)$$

Here, functions  $f(x)$  and  $f_E(x)$  define the mass profiles for NFW and Einasto approximations correspondingly, and  $C$



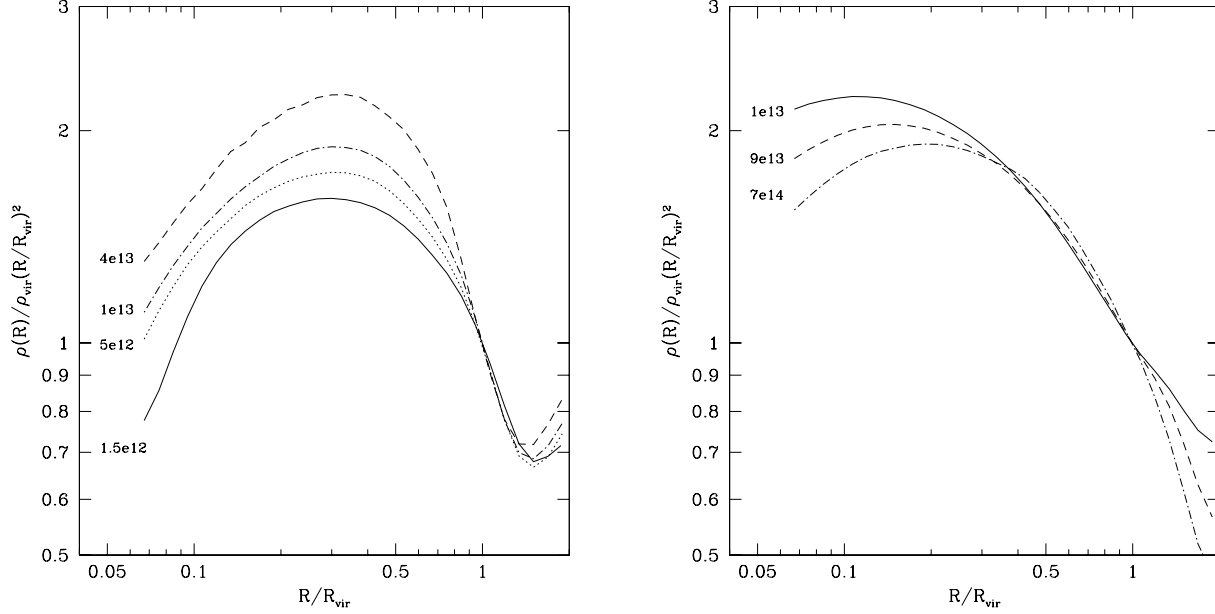


**Figure 9.** Median density profiles of relaxed halos at different redshifts and masses in the MDPL simulation. Profiles are normalized to have the same density at the virial radius. The left panel is for halos at  $z = 3$ : halos with larger mass are clearly more concentrated than halos with smaller masses. Similar to Einasto profiles in Figure 6, value of  $r_{-2}$  radius almost does not change with halo mass, which indicates that the increase in the concentration is mostly due to the increase in shape parameter  $\alpha$ . The right panel shows profiles of halos at  $z = 0$ . Note that the trend with mass is different: more massive halos are less concentrated and  $r_{-2}$  radius decreases with decreasing mass.

and  $C_E$  are formal halo concentrations. Using these relations one can find the radius  $x_{\max}$  at the maximum of the circular velocity,  $V_{\max}$ .

Once  $V_{\max}/V_{\text{vir}}$  ratio is measured in simulations, it can be used to estimate the formal concentration  $R_{\text{vir}}/r_{-2}$ . For the Einasto approximation one can use one of the two relations in eq. (14):

$$\frac{V_{\text{circ}}^2(r)}{V_{\text{vir}}^2} = \frac{C_E}{x_{\max}} \frac{f_E(x_{\max}, \alpha)}{f_E(C_E, \alpha)}, \quad (18)$$

$$x_{\max} \approx 3.15 \exp(-0.64\alpha^{1/3}) \quad (19)$$

And for the NFW profile:

$$\frac{V_{\text{circ}}^2(r)}{V_{\text{vir}}^2} = \frac{C}{x_{\max}} \frac{f(x_{\max})}{f(C)}, \quad x_{\max} = 2.163 \quad (20)$$

It is convenient to cast the  $V_{\max}/V_{\text{vir}}$  ratio into the concentration using the NFW profile. For this we use eq. (19) to convert the velocity ratio into concentration  $C$ . For halos that can be approximated by the NFW profile – and vast majority of them are – this gives us the familiar relation  $C = R_{\text{vir}}/r_{-2}$ . For high- $\nu$  halos that are not approximated by the NFW profile, this still gives a measure of concentration: the larger  $C$  the more dense is the central region of these halos. Because the mapping from the  $V_{\max}/V_{\text{vir}}$  ratio to the concentration  $C$  is monotonic, it always can be inverted to recover  $V_{\max}/V_{\text{vir}}$  and then to find  $R_{\text{vir}}/r_{-2}$  for halo with given parameter  $\alpha$ .

The BDM halofinder provides measurements of  $V_{\max}$  and  $V_{\text{vir}}$  for each halo, which are converted to estimates of concentration  $C$ . When studying dependence of concentration on mass or  $V_{\max}$ , we bin halos according to their mass or  $V_{\max}$ . Halos in each bin (typically many thousands) are

ranked by their values of  $C$  and median values and deviations from the mean are found.

Similar procedure is used for dark matter profiles or profiles of the radial infall velocities and velocity anisotropy parameter  $\beta$ . We normalize radii to the virial radius of each halo. Then profiles are binned using constant bin size in logarithm of radius  $\Delta R/R_{\text{vir}} = 0.05$ . Radii are binned from  $\sim 5\%$  of  $R_{\text{vir}}$  to  $2R_{\text{vir}}$ . For each radial bin, values from individual halos are ranked from the smallest to the largest and medians and deviations are found.

## 5 HALO PROFILES AT DIFFERENT REDSHIFTS

Some of halos in our simulations are resolved with millions of particles, but a vast majority have just few thousands. For this paper our goal is to study these numerous halos that are resolved from modest radius  $\sim 0.05R_{\text{vir}}$  to  $2R_{\text{vir}}$ . Simulations provide us the density profiles and also profiles of velocity dispersions, velocity anisotropies and radial infall velocities. Because of the wealth of information, we cannot show all combinations of halo profiles. Instead, we show only representative results.

One of the interesting issues is the structure of high- $\nu$  halos and the upturn in halo concentrations. In order to avoid possible complications with on-going major-mergers, we start the analysis with density profiles of relaxed halos. We select halos in a narrow range of masses and normalize distances by the virial radius and normalize densities by the density at the virial radius. Even with the narrow mass bins the number of halos in each bin is so large that the



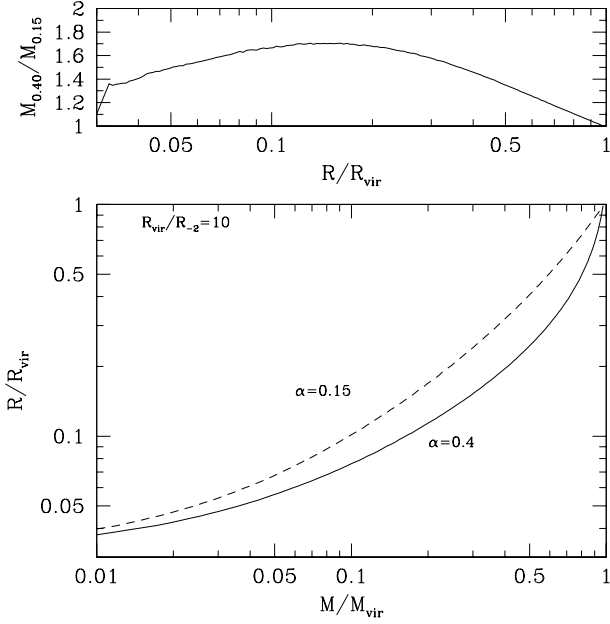


**Figure 8.** Comparison of two Einasto profiles with the same mass  $M_{\text{vir}}$ , virial radius  $R_{\text{vir}}$  and core radius  $r_{-2} = 0.1R_{\text{vir}}$ . The bottom plot shows the radius encompassing the same fraction of mass. The top panel presents the ratio of masses within the same radius (top panel) for two Einasto profiles with shape parameters  $\alpha = 0.15$  and  $\alpha = 0.40$ . All the statistics indicate that the  $\alpha = 0.4$  profile is more concentrated in spite of having the same formal concentration. The plot illustrates that the concentration of the Einasto profile depends on both the core radius  $r_{-2}$  and the shape parameter  $\alpha$ .

statistical errors of median values are very small. This is the reason why we do not show any statistical error bars in our plots.

The right panel Figure 9 shows density profiles for relaxed halos at  $z = 0$ . Even without fitting profiles with either NFW or Einasto profiles, the figure shows the well known trend with mass: more massive halos are less concentrated than the less massive ones. This can be seen by comparing densities at, say  $R \approx 0.1R_{\text{vir}}$ . There is another trend: the radius at which the density declines as  $\rho \propto R^{-2}$  (radius where curves in the plot are horizontal) increases with increasing mass. While the halos in the plot have large mass, in the sense of peak height they are not large:  $\nu = 1 - 2.8$ .

Halos at larger redshifts demonstrate strikingly different profiles. The left panel in Figure 9 presents halos at  $z = 3$ . Here the trend with mass is very different with more massive halos being more concentrated. There is a number of ways to demonstrate this. For example, inside a given fraction of virial radius  $R/R_{\text{vir}}$  larger halos have larger fraction of halo mass. Also the radius containing a given fraction of mass (another measure of concentration) is smaller for more massive halos. Another change in the halo profiles is the radius with the log-log slope -2 for density profiles. For these halos there is very little dependence of  $R_{\text{vir}}/R_{-2}$  on halo mass.

Note that the halos at  $z = 3$  shown in the right panel of Figure 9 represent very large density peaks:  $\nu = 2.6 - 4.5$ . Indeed, it is mostly the height of the peak that defines the

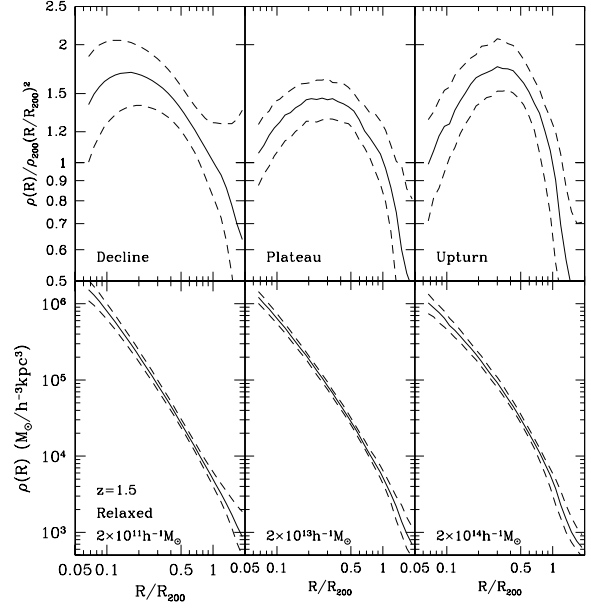


**Figure 10.** Median halo profiles (full curves) of relaxed halos in different dynamical regimes. All halos are selected at  $z = 1.5$ . Dashed curves show  $1\sigma$  deviations from the median. Left panels show halos in the declining part for concentration-mass  $c(M)$  relation. The middle panels are for halo close to the minimum of  $c(M)$ , and the right panels show halos in the upturn. Top panels show density profiles multiplied by the square of radius and normalized to the density at the virial radius. Halos in the declining  $c(M)$  regime are more concentrated than halos in the “plateau”, which can be judged by slightly larger densities in the central  $R \lesssim 0.1R_{200}$  region and by smaller radius where  $R^2\rho(R)$  reaches the maximum. Halos in the upturn are denser than at the plateau, but in a different way: they have larger density in intermediate radii  $R/R_{200} \approx (0.2 - 0.5)$  and the radius of their peak of  $R^2\rho(R)$  does not change.

change in the structure of halo profiles. As we will see later, there is a dependence with the redshift, but this appears to be a weaker factor shaping the structure of halos with peak height being the dominant effect. We can demonstrate this by selecting halos at the same redshift but with different  $\nu$ .

For that we select relaxed halos at  $z = 1.5$ . The first sample of halos has mass  $M_{\text{vir}} = 2 \times 10^{11} h^{-1} M_{\odot}$  and  $\nu = 1.1$ . These halos are in the regime of declining concentration-mass relation  $C(M)$ . Halos in the regime of the flat part of the  $C(M)$  are represented by halos with  $M_{\text{vir}} = 2 \times 10^{13} h^{-1} M_{\odot}$  and  $\nu = 2.5$  and the upturn of the  $C(M)$  is represented by  $M_{\text{vir}} = 2 \times 10^{14} h^{-1} M_{\odot}$  and  $\nu = 4.1$ . Profiles of these three types of halos are shown in Figure 10. Halos in the plateau of the  $C(M)$  have the lowest concentration and halos in the declining and upturn regimes are more concentrated. There is also a change in the shape of the density profiles. For example, the  $r^2\rho(r)$  curves are broader for plateau halos and are more narrow for the upturn halos.

Figure 10 also shows rms deviations from the median profiles of halos. There is not much difference between different populations of halos. In this respect rare halos at the upturn are not more violent and do not have larger spread of

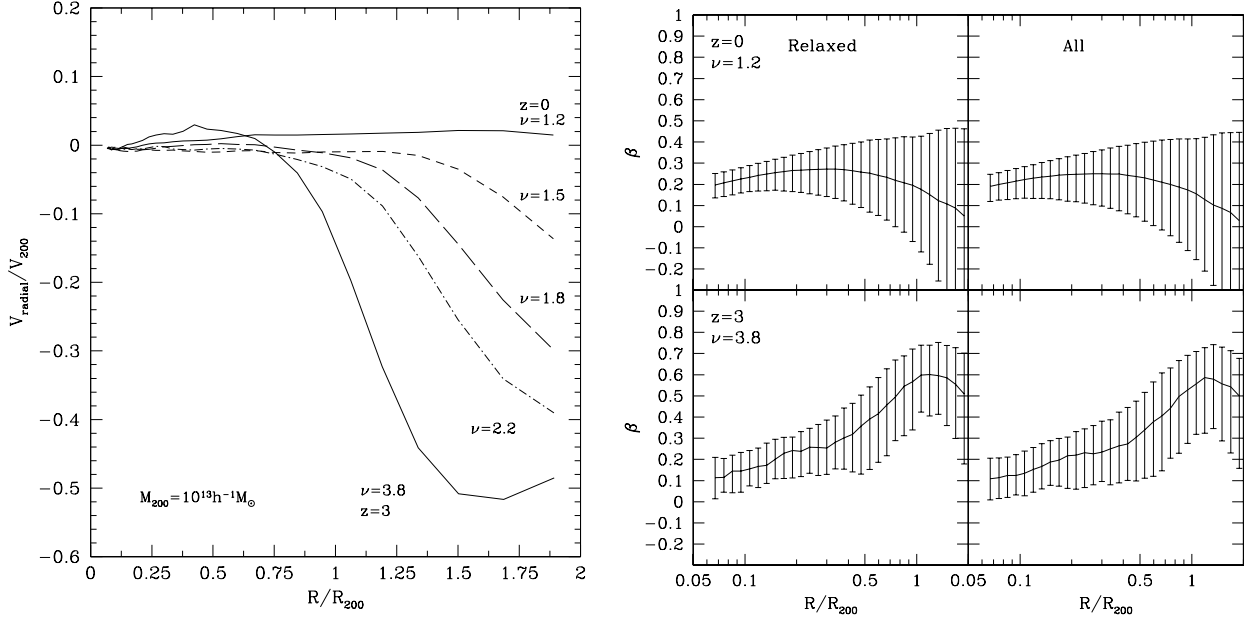


**Figure 11.** Velocity structure of halos with mass  $M_{200} = 10^{13} h^{-1} M_{\odot}$  at different redshifts. *Left panel:* Median radial velocity profiles of relaxed halos at redshifts  $z = 0, 0.5, 1, 1.5, 3$  (from top to bottom). Halos with a constant mass represent density peaks of different height  $\nu$  as indicated in the plot. There are large infall velocities ( $V_{\text{radial}} \approx 0.5V_{200}$ ) just outside the virial radius for high- $\nu$  halos, which changes to almost no infall for  $\nu \lesssim 1$ . The inner regions of all halos clearly indicate relaxation with the median radial velocity being very close to zero for both relaxed and unrelaxed halos. *Right panel:* Velocity anisotropy parameter  $\beta$  for halos with virial mass  $M_{200} = 10^{13} h^{-1} M_{\odot}$  for redshift  $z = 0$  (top panels) and  $z = 3$  (bottom panels). Relaxed halos were used for plots in left panels and all halos were used for right panels. Error bars indicate  $1\sigma$  deviations from the mean. At  $z = 0$  these halos represent low- $\nu$  peaks in density fluctuations. They are in “normal” declining  $c(M)$  regime. Halos have slightly radial orbits of dark matter particles with nearly constant  $\beta \approx 0.2$ . At  $z = 3$  the halos with the same mass are high- $\nu$  peaks in the upturn regime of  $c(M)$ . Orbits are very radial in the outer halo regions with  $\beta \approx 0.5$  at  $R_{200}$ . Note that there is almost no difference between all and relaxed halos in spite of the fact that at  $z = 3$  only 1/3 of halos are considered relaxed.

densities as compared with “normal” halos of the declining  $C(M)$  population. However, many other halo properties do depend on  $\nu$ .

Figure 11 shows radial velocity profiles  $V_{\text{radial}}$  normalized to the virial velocity and the velocity anisotropy parameter  $\beta$  for halos with  $M_{200} = 10^{13} h^{-1} M_{\odot}$  at different redshifts and different peak heights  $\nu$ . Nearly zero infall velocities  $V_{\text{radial}} \approx 0$  indicate that central regions of halos  $R \lesssim R_{200}$  are close to equilibrium at all times. This is true even for  $z = 3$  halos that are at the upturn regime of the  $C(M)$  relation. This confirms our estimates of the virial parameter  $2K/|W| - 1$  in Sec. 3: corrected for the surface pressure the virial parameter is close to zero.

Negative  $V_{\text{radial}}$  values at radii larger than the virial radius indicate that matter falls into the halos resulting in its mass growth. However, the magnitude of the infalling velocities drastically depends on  $\nu$ . It is nearly a half of the circular velocity at the virial radius for  $\nu > 3$  and goes to almost zero for  $\nu \lesssim 1$  (Prada et al. 2006; Cuesta et al. 2008; Diemer et al. 2013). Large infall velocities on high- $\nu$  halos are accompanied by very radial velocity anisotropy as demonstrated by right panels in Figure 11.

In order to characterize the density profiles of halos at different redshifts, masses and different  $\nu$ , we stack profiles of halos binned by mass and normalize radii by virial radius of each halo. The number of halos in each mass bin is many hundreds and often thousands. We use only halos with more

than 5000 particles. We then fit the Einasto profile eq.(12) using *two* free parameters:  $r_{-2}$  and  $\alpha$ . The third parameter is fixed to produce the total mass corresponding to the mass of selected halos. We note that this is not what is usually done (e.g., Macciò et al. 2007; Gao et al. 2008; Dutton & Macciò 2014). Usually all three parameters are considered as free. This cannot be correct once the total mass is fixed by selecting halos by mass.

Parameters  $\alpha$  and  $r_{-2}$  of all halos in the Planck cosmology simulations SMDPL, MDPL, and bigMDPL are presented in Figure 12. Dependence of  $\alpha$  and  $R_{200}/r_{-2}$  on the peak height can be approximated with the following expressions:

$$\alpha = 0.115 + 0.0165\nu^2, \quad (21)$$

$$R_{200}/r_{-2} = 6.5\nu^{-1.6} (1 + 0.21\nu^2), \quad (22)$$

For relaxed halos we find that  $\alpha$  parameter is slightly smaller for high- $\nu$  halos and can be approximated as:

$$\alpha = 0.115 + 0.0140\nu^2. \quad (23)$$

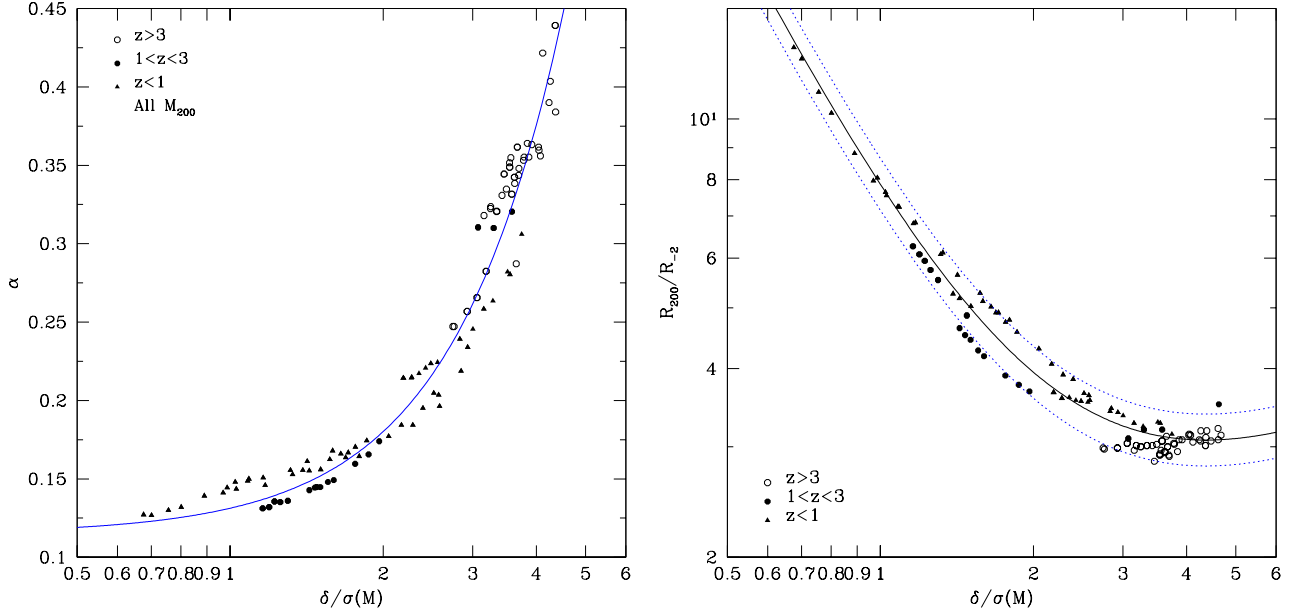


**Figure 12.** Dependence of the structural parameter  $\alpha$  (left panel) and the ratio of the virial radius  $R_{200}$  to the Einasto core radius  $r_{-2}$  (right panel) on the peak height  $\nu = \delta_{\text{cr}}/\sigma(M, z)$ . All halos in simulations with the Planck cosmology were used for this analysis. The full curves show the analytical approximations eqs.(22). The dotted curves in the right panel indicate 10% deviations from it.

## 6 HALO CONCENTRATIONS: EVOLUTION WITH REDSHIFT

In addition to cosmological parameters, redshift, mass, and definition of virial radius, the halo concentration depends on how halos are selected. There are a number of options to do that. One can select all halos or only relaxed halos. Halos can be selected by virial mass or by circular velocity. Not surprisingly, different selection options result in a large number of combinations of  $C(M)$  approximations. However, *qualitatively* the results are the same. Figure 13 gives two examples of  $C(M, z)$  for halos selected in different ways. Here, we show the evolution of halo concentration defined using eq. (19) for halos selected by  $V_{\text{max}}$  and by  $M_{200}$ . The plots illustrate a well known result that the evolution of  $C(M, z)$  is quite complex (e.g. Prada et al. 2012). Nevertheless, qualitatively the pattern of the evolution is the same regardless how halos are selected.

The plots in Figure 13 show that there are three regimes for  $C(M)$ : a declining part on small masses, an upturn at very large masses and a plateau in between. Curves for  $z = 1$  and  $z = 2.5$  clearly illustrate this behavior. There is no declining part of  $C(M)$  at very large redshifts because our simulations do not have enough resolution to probe the declining branch of  $C(M, z)$ .

As discussed in the previous section, the upturn in the concentration is related with the increase of  $\alpha(M)$  at large masses. This is different for halos in the declining regime where the concentration declines mostly due to the change in the core radius  $r_{-2}$  while  $\alpha(M)$  stays nearly constant.

There is no upturn at  $z = 0$ . In order to shed light on this, we explore the evolution of halo concentration at low redshifts. Figure 14 shows that the concentration on the plateau starts to decline at  $z \approx 0.5$  and the upturn gets smaller and disappears at  $z = 0$ . Though the reason is not

**Table 2.** Parameters for the concentration - mass relation given by eq.(24) for the Planck cosmology. Halos are defined using the overdensity  $200\rho_{\text{mcr}}$  criterion. All halos are selected by mass.

Redshift	Parameter		
	$C_0$	$\gamma$	$M_0/10^{12}h^{-1}M_\odot$
0.00	7.40	0.120	$5.5 \times 10^5$
0.35	6.25	0.117	$1.0 \times 10^5$
0.50	5.65	0.115	$2.0 \times 10^4$
1.00	4.30	0.110	900
1.44	3.53	0.095	300
2.15	2.70	0.085	42
2.50	2.42	0.080	17
2.90	2.20	0.080	8.5
4.10	1.92	0.080	2.0
5.40	1.65	0.080	0.3

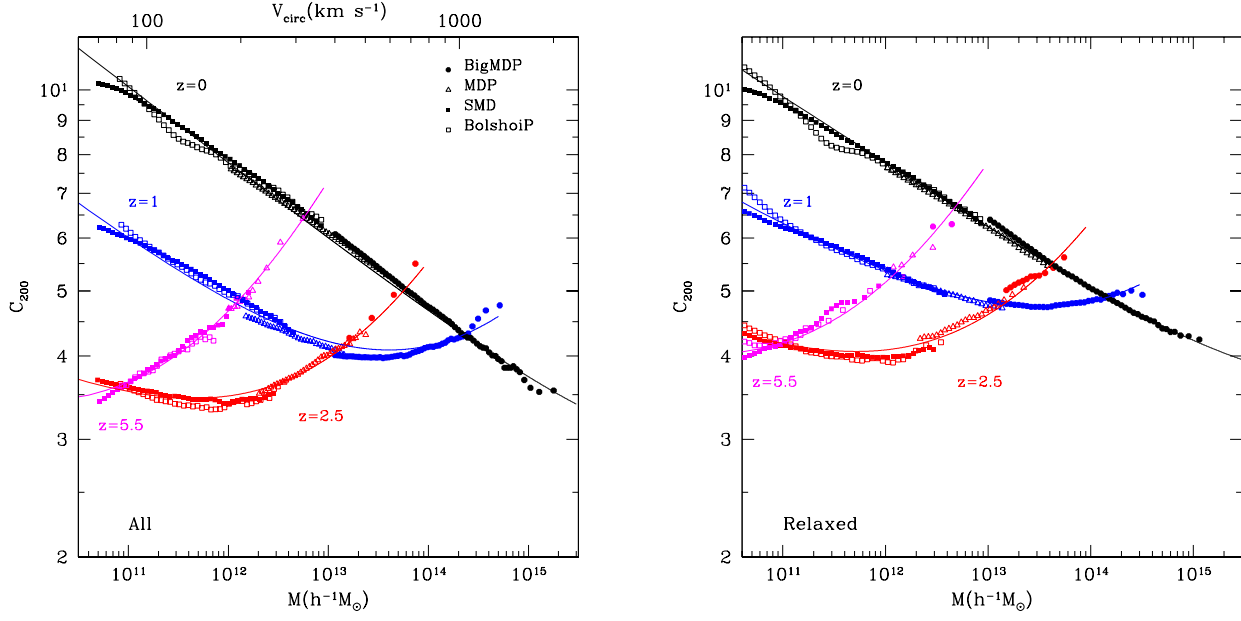
exactly clear, we speculate that this likely is related with the decline in matter density  $\Omega_m(z)$  and, consequently, slower mass accretion on halos.

It is often convenient to have simple fits for concentration as function of mass for some redshifts. To make those fits we use the following 3-parameter functional form:

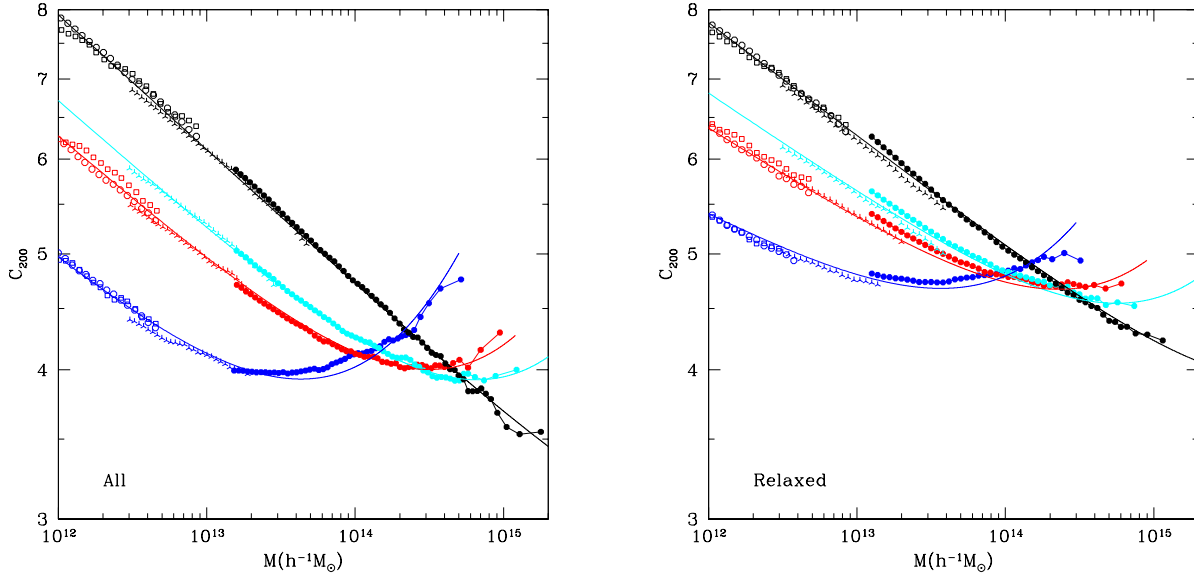
$$C(M) = C_0 \left( \frac{M}{10^{12}h^{-1}M_\odot} \right)^{-\gamma} \left[ 1 + \left( \frac{M}{M_0} \right)^{0.4} \right]. \quad (24)$$

Table 2 gives parameters  $C_0$  and  $M_0$  for this approximation for the Planck cosmology. Parameters for additional selection conditions and for WMAP7 cosmology are presented in the Appendix in tables A1– A4.

Following Prada et al. (2012) we study the evolution of halo concentrations as function of the amplitude of perturbations  $\sigma(M)$  or as function of peak height  $\nu(M)$ . Evolution



**Figure 13.** Examples of the evolution of halo concentration in the MultiDark suite of simulations. Here we show results for simulations with the Planck cosmological parameters. The overdensity 200 criterion was used to find virial mass and radius. *Left panel:* All halos are binned by the maximum circular velocity  $V_{\text{max}}$ . Bottom axis presents corresponding average virial mass of these halos. *Right panel:* Relaxed halos are binned by virial mass. Full curves in the plots show fits given by eq.(24). Relaxed halos have larger concentrations and shallower slopes at small masses. Qualitatively the evolution of halo concentration does not depend on selection of halos.



**Figure 14.** The same as in Figure 13 but for low redshifts. In each panel from top to bottom results are presented for redshifts  $z = 0, 0.35, 0.5, 1$ . The plot shows how the upturn in  $c(M)$  seen at high redshifts gradually disappears as the Universe becomes dominated by the dark energy.

of the  $C(\nu)$  relation for halos defined using the virial mass  $M_{\text{vir}}$  and radius  $R_{\text{vir}}$  is presented in Figure 15 for the Planck cosmology for all and relaxed halos. As Figure 15 shows, the evolution of  $C(\nu)$  looks more simple as compared with  $C(M, z)$ . As Prada et al. (2012) and Diemer & Kravtsov

(2014b) found, the shape of  $C(\nu)$  is almost the same at every redshift, but its position in the  $C - \nu$  diagram gradually shifts. Here we find that the following functional form de-

scribes the shape of  $C(\nu)$ :

$$C(\sigma) = b_0 \left[ 1 + 7.37 \left( \frac{\sigma}{a_0} \right)^{3/4} \right] \left[ 1 + 0.14 \left( \frac{\sigma}{a_0} \right)^{-2} \right] \quad (25)$$

Parameters  $b_0$  and  $a_0$  for different redshifts and selection conditions are given in the Appendix in tables A5 and A6.

## 7 UPTURN OF HALO CONCENTRATION

The upturn in the concentration – mass relation is probably the most controversial regime. It was first discovered in Klypin et al. (2011) in the Bolshoi simulation made with the ART code. It later was found in the Millennium GADGET simulations and in the ART Multidark simulation by Prada et al. (2012) who made extensive analysis of halos at the upturn.

Considering that the upturn is a relatively new feature, some “explanations” were proposed why the upturn is not real. Ludlow et al. (2012) argue that the upturn is an artifact of halos that are out of equilibrium. Their idea can be summarized as follows. The most massive halos grow fast. When those halos are caught in the process of first major merger, the infalling satellite penetrates deep into the major halo producing an illusion of a very concentrated halo. When Ludlow et al. (2012) removed halos, which they perceived to be unrelaxed, they find that there is no upturn. The problem with this idea is that Ludlow et al. (2012) did not make the pressure term correction to the virial ratio. This renders most of the most massive halos to be considered unrelaxed when they actually are. The lack of infalling (radial) velocities in the central region of  $\sim 1/3$  of the virial radius is also not consistent with the idea of “first infall” as an explanation for the upturn. So, the non-equilibrium explanation for the upturn does not seem to be valid.

Another idea for the upturn is related with the fact that in Klypin et al. (2011) and Prada et al. (2012) the concentration was estimated using the  $V_{\max}/V_{\text{vir}}$  ratio. So, one may speculate that the upturn is due to the procedure. However, Prada et al. (2012) and more recently Dutton & Macciò (2014) compare estimates of concentration done with fitting the NFW profiles and with the  $V_{\max}/V_{\text{vir}}$  ratio. They find that both methods produce nearly identical results for most of halos. Systematic  $\sim 10\%$  differences in concentration were found only for the most massive halos. However, the problem with the fitting densities of the massive halos is that the profiles substantially deviate from the NFW profile. For these halos only the ratio  $R_{\text{vir}}/r_{-2}$  was reported as a concentration, thus missing the main contribution to the concentration, i.e. the increase of  $\alpha$ .

The properties of halos at the upturn point into a different explanation for the origin of the upturn. These extremely massive halos form around very high density peaks of initial linear density perturbations. The analysis of statistical properties of gaussian random fields shows that these rare peaks tend to be more spherical than low- $\nu$  peaks (Doroshkevich 1970; Bardeen et al. 1986). In turn, this means that infall velocities are also more radial resulting in deeper penetration of infalling mass into the halo. This produces more centrally concentrated halos.

This large concentration will not be preserved as more material is accreted. As the mass grows, the relative peak height becomes lower and the infall velocities become less radial. The halo gradually slides into the plateau regime. As the rate of accretion decreases even more, the central region stops to be severely affected by mergers, which now tend to build more extended outer regions. This will be the “normal” slow growth mode of halos and associated with the decline regime in the concentration – mass relation.

## 8 COMPARISON WITH OTHER RESULTS

There are some differences between our results with those in Prada et al. (2012). We now have more data, which allow us to make more detailed analysis of concentrations. We also make fits of density profiles using the Einasto profiles. In Prada et al. (2012) we used only bound particles to estimate profiles and concentrations. Even for the most massive halos the average fraction of unbound particles is less than  $\sim 3\%$ . However, this increases the halo concentration by as much as  $\sim 10\%$ .

We start with comparing different published estimates of halo concentrations at redshift  $z = 0$ . In the left panel of Figure 16 we compare different published results of concentrations defined using the NFW profiles for all halos in the WMAP5/7 cosmologies. Overall, the agreement between different groups is quite reasonable, but there some systematic difference. For example, results of Duffy et al. (2008) and Macciò et al. (2008) are systematically below our estimates by  $\sim 10\%$ . Concentrations in Diemer & Kravtsov (2014a) are  $\sim 5\%$  above ours. They also find some indication of an upturn at the largest masses, which we do not see in our simulations.

We compare concentrations for the Planck cosmology at different redshifts in the right panel of Figure 16. Here, we compare NFW-based concentrations for relaxed halos in our simulations with those in Dutton & Macciò (2014). There is an excellent agreement for  $z = 0$  with deviations less than  $\sim 2\%$ . The situation is more complicated at high redshifts with again very good agreement at low masses and substantial differences at large masses. However, one should remember that Dutton & Macciò (2014) fit the NFW profiles to the data and we do not. Because the most massive halos at high redshifts have large deviations from the NFW profiles, not surprisingly we have large differences between our estimates and those of Dutton & Macciò (2014).

Because halo concentrations are used to estimate density profiles, it is important to compare different predictions for dark matter density profiles, not just concentrations. We give two examples of such a comparison. In the right panel of Figure 17 we show the median density profile of all halos at redshift  $z = 1$  with mass  $M_{200} = 10^{14} h^{-1} M_{\odot}$  in the WMAP7 MultiDark simulation. The black thin curve also shows our approximation using the Einasto profile with parameters defined by eqs.(21-23). We also compare our results with the predictions given in Table 1 of Duffy et al. (2008) for both NFW and Einasto profiles. Those predictions are systematically below the results of simulations by  $\sim 10\%$ . Note that the problem cannot be fixed by scaling up the density profiles to improve the accuracy of the fits. This

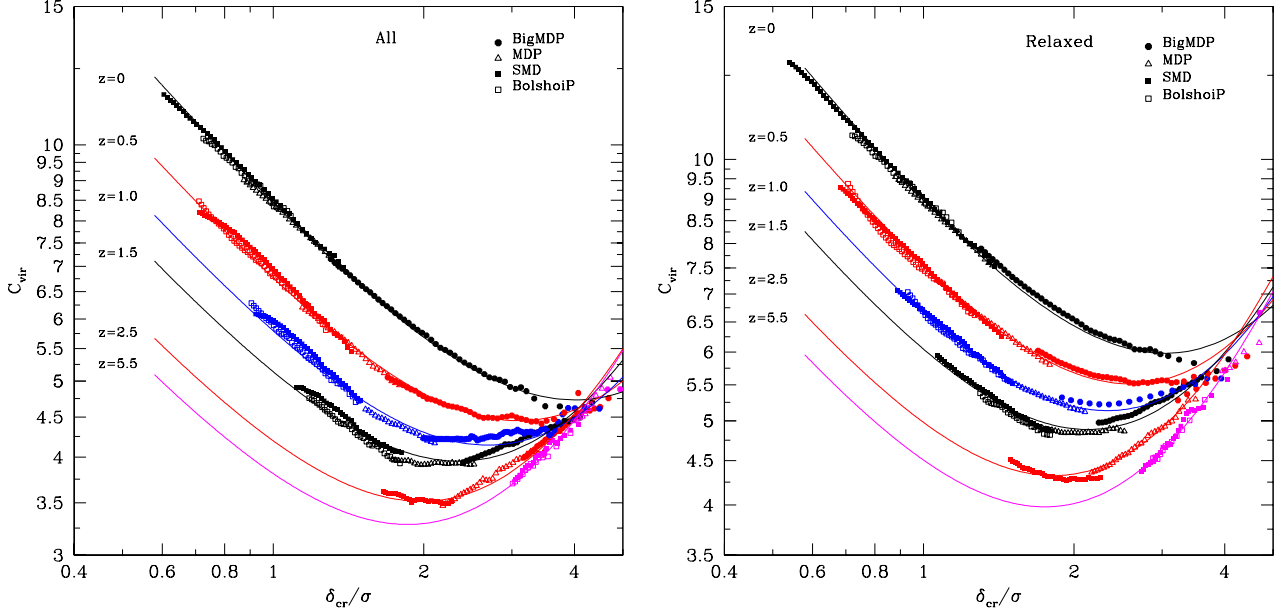


**Figure 15.** Dependence of halo concentration on the peak height  $\nu = \delta_{\text{cr}}/\sigma(M, z)$  for all halos (left panel) and relaxed halos (right panel). Full curves show analytical fits given by eq. (25).

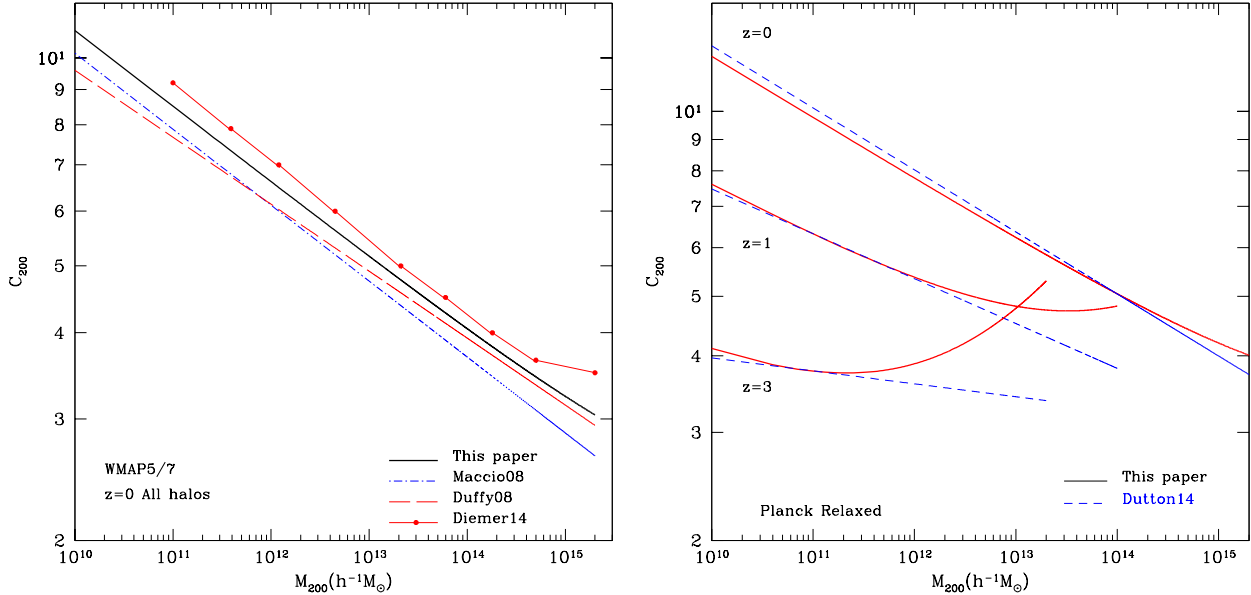


**Figure 16.** Comparison of predictions of dark matter halo concentrations defined using the NFW profiles. *Left:* Comparison of different published results of concentrations for all halos in the WMAP5/7 cosmologies. Overall the agreement between different groups is quite reasonable, but there are some systematic differences. Results of Duffy et al. (2008) and Macciò et al. (2008) are systematically below our estimates by  $\sim 10\%$ . Concentrations in Diemer & Kravtsov (2014a) are  $\sim 5\%$  above ours. *Right:* Comparison of concentrations of relaxed halos in simulations with the Planck cosmology at different redshifts. Agreement between our results and those of Dutton & Macciò (2014) is very good for  $z = 0$  and for small masses at high redshifts. Disagreement at large masses is due to fitting NFW profiles to halos that substantially deviate from the NFW shape. Agreement improves once the Einasto profiles are used.

cannot be done because the total halo mass will be substantially larger than the mass of the halo in the simulation.

The failure of the Einasto fit in the Duffy et al. (2008) approximation is related to their approximation for the  $\alpha(\nu)$  parameter. Duffy et al. (2008) used results from Gao et al.

(2008) (eq. 13) that gives a  $\sim 10\%$  smaller value of  $\alpha$  as compared with our estimate given by eq. (21). Combined with a slightly smaller value of the formal concentration, this results in the halo density profile, which is systematically misses by  $\sim 10\%$  the density in the simulation.

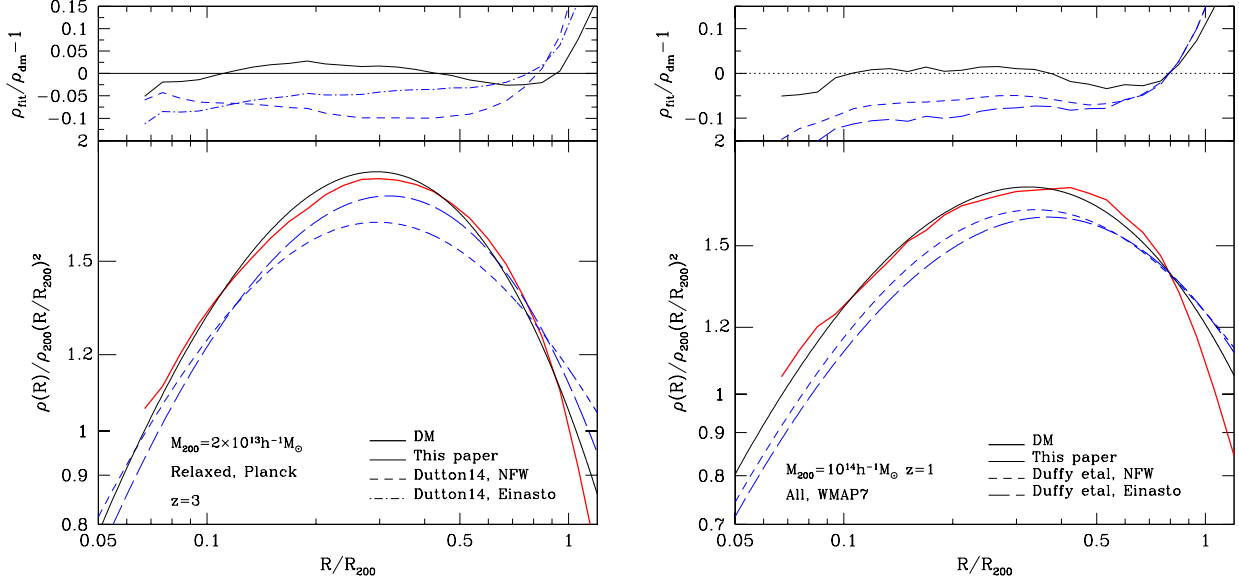


**Figure 17.** Comparison of predictions of halo density profiles at different redshifts. Full thick curves in both panels show density profiles multiplied by radius squared and normalized to the density at  $R_{200}$ . Top panels show errors of different approximations. Approximations are normalized to have the same mass as the dark matter halos. *Left:* Profiles for relaxed halos in the Planck cosmology simulations with mass  $M_{200} = 2 \cdot 10^{13} h^{-1} M_{\odot}$  at  $z = 3$ . Short and long dashed curves show predictions for the NFW and Einasto profiles by Dutton & Macciò (2014).

Comparison of our density profiles with those by Dutton & Macciò (2014) shows much better agreement as indicated in the left panel of Figure 17 when the Einasto profile is used. Here, we show density profile for relaxed halos with  $M_{200} = 2 \cdot 10^{14} h^{-1} M_{\odot}$  in the Planck cosmology simulation MDPL at  $z = 3$ . The total of  $\sim 300$  halos were used to produce the median profile. Halos of this mass and redshift have  $\nu = 3.9$ , which puts them in the upturn of the concentration - mass relation. Our analytical fit for the density profile is obtained using eq. (23) for the  $\alpha$  parameter. The  $R_{200}/r_{-2}$  ratio is estimated using eq. (22), which we scale up by factor 1.1 to account for the fact that relaxed halos are more concentrated than all halos. To construct profiles predicted by Dutton & Macciò (2014), we use parameters for the NFW and Einasto approximations from their Table 3. All analytical fits are normalized to have the same total halo mass.

It is clear that the NFW fit given by Dutton & Macciò (2014) provides a halo, which is less concentrated than that in the simulation. This is consistent with the differences which we saw in the right panel of Figure 16: the NFW fits predict too low concentrations for halos at the upturn resulting in  $\sim 10\%$  too low densities. However, the differences between our and Dutton & Macciò (2014) Einasto fits are significantly smaller.

## 9 HOW TO ESTIMATE DENSITY PROFILES

We offer different options to estimate density profiles of dark matter halos. Halos in the declining branch of the  $C(M, z)$  relation ( $\nu \lesssim 2$ ) can be approximated using the NFW profile. Tables in the Appendix give numerous parameters for halos

selected in different ways. One can interpolate between the values provided by the Tables to find the approximations for different redshifts. The interpolation of  $C(\nu)$  parameters is expected to be more accurate because there is less evolution of the parameters with the redshift.

There are two options for handling halos at the plateau and upturn. For all halos in the Planck cosmology one can use eqs.(21-22) to find  $\alpha$  and  $R_{200}/r_{-2}$ . For other selection conditions and for the WMAP cosmology, one should use eqs.(21) or eqs.(23) to find  $\alpha$ . These relations are expected to be least dependent on details of selection and cosmological parameters. Then one should use one of the approximations for  $C(\sigma)$  given in the Appendix. Finally, solve eqs.(18-20) to find  $C_E \equiv R_{200}/r_{-2}$  for known  $C$  and  $\alpha$ .

## 10 CONCLUSIONS

In this paper we present the new suite of MultiDark cosmological N-body simulations from which we have identified more than 60 billion dark matter halos that span more than 5 orders of magnitude in mass and covers more than  $50 \text{ Gpc}^3$  in volume. From this large data set we have studied with very high accuracy the halo density, infall velocity and velocity anisotropy profiles and concentrations in three dynamical regimes: declining concentration, plateau, and upturn. We derive analytical approximations that provide 2–5% accurate estimates for halo concentrations and density profiles.

We summarize the main results from this work:

- In order to understand the evolution of halo concentration and, specifically the nature of the upturn, one needs to realize that the halo concentration is not defined as the



ratio of the virial radius to the radius  $r_{-2}$  as in the NFW profile. For massive halos the average density profile is far from the NFW shape and the concentration is not defined by the core radius  $r^{-2}$ . In Section 5 we present density profiles that clearly show that massive halos at  $z = 3$  have increasing concentrations with increasing mass and they have nearly unchanging  $R_{\text{vir}}/r_{-2}$ . Both parameters  $\alpha$  and  $r_{-2}$  of the Einasto approximation affect the concentration.

- We speculate that the increase in the halo concentrations for the most massive halos is related with the tendency of rare peaks in the random gaussian linear density field to be more spherical (Doroshkevich 1970; Bardeen et al. 1986). Very radial accretion onto these peaks is clearly seen in Figure 11 with the average velocity anisotropy parameter  $\beta = 0.5 - 0.7$  for halos with  $\nu \approx 4$ . This radial infall brings mass closer to the center, producing a highly concentrated halo. As time goes on the halo slides into the plateau regime, and accretion becomes less radial. Now mass is deposited at larger radius, and the concentration declines. Once the rate of accretion and merging slows down, the halo moves into the domain of declining  $C(M)$  because new accretion piles up mass close to the virial radius while the core radius is staying constant.

- The ratio of the maximum circular velocity to the virial velocity  $V_{\text{max}}/V_{\text{vir}}$  gives a profile-independent measure of the halo concentration.

- Density profiles of very massive halos with  $\nu > 3$  substantially deviate from the NFW shape. Fitting an NFW profile for these halos gives incorrect results regardless on how the fitting (what range of radii) is done. The differences between the NFW and Einasto concentrations for these massive halos do not mean that there are uncertainties in halo concentration. They simply indicate that the NFW formula should not be used.

- Differences between the  $V_{\text{max}}/V_{\text{vir}}$  concentration and the formal concentration obtained by fitting the Einasto profile (the ratio  $R_{\text{vir}}/r_{-2}$ ) do not indicate that there are real disagreements. These two estimates are for different quantities. The  $R_{\text{vir}}/r_{-2}$  ratio is only a part of the real halo concentration.

## ACKNOWLEDGEMENTS

The BigMultidark simulations have been performed on the SuperMUC supercomputer at the Leibniz-Rechenzentrum (LRZ) in Munich, using the computing resources awarded to the PRACE project number 2012060963. Bolshoi(P) and MultiDark simulations were performed on Pleiades supercomputer at the NASA Ames supercomputer center. S. H. wants to thank R. Wojtak for useful discussions. The authors want to thank V. Springel for providing us with the optimized version of GADGET-2. S.H. acknowledges support by the Deutsche Forschungsgemeinschaft under the grant GO563/21-1. A.K. acknowledges support of NSF grants to NMSU. GY acknowledges support from MINECO (Spain) under research grants AYA2012-31101 and FPA2012-34694 and Consolider Ingenio SyeC CSD2007-0050 F.P. acknowledges support from the Spanish MICINN Consolider-Ingenio 2010 Programme under grant MultiDark CSD2009-00064, AYA2010-21231-C02-01, and MINECO Centro de

Excelencia Severo Ochoa Programme under grant SEV-2012-0249.

## REFERENCES

- Alimi J.-M. et al., 2012, ArXiv e-prints 1206.2838  
 Angulo R. E., Springel V., White S. D. M., Jenkins A., Baugh C. M., Frenk C. S., 2012, MNRAS, 426, 2046  
 Angulo R. E., White S. D. M., 2010, MNRAS, 405, 143  
 Bardeen J. M., Bond J. R., Kaiser N., Szalay A. S., 1986, ApJ, 304, 15  
 Behroozi P. S., Wechsler R. H., Wu H.-Y., 2013, ApJ, 762, 109  
 Bryan G. L., Norman M. L., 1998, ApJ, 495, 80  
 Bullock J. S., Kolatt T. S., Sigad Y., Somerville R. S., Kravtsov A. V., Klypin A. A., Primack J. R., Dekel A., 2001, MNRAS, 321, 559  
 Crocce M., Fosalba P., Castander F. J., Gaztañaga E., 2010, MNRAS, 403, 1353  
 Cuesta A. J., Prada F., Klypin A., Moles M., 2008, MNRAS, 389, 385  
 Davis A. J., D'Aloisio A., Natarajan P., 2011, MNRAS, 416, 242  
 Diemer B., Kravtsov A. V., 2014a, ArXiv e-prints  
 Diemer B., Kravtsov A. V., 2014b, ArXiv e-prints  
 Diemer B., More S., Kravtsov A. V., 2013, ApJ, 766, 25  
 Doroshkevich A. G., 1970, Astrophysics, 6, 320  
 Duffy A. R., Schaye J., Kay S. T., Dalla Vecchia C., 2008, MNRAS, 390, L64  
 Dutton A. A., Macciò A. V., 2014, MNRAS, 441, 3359  
 Einasto J., 1965, Trudy Astrofizicheskogo Instituta Alma-Ata, 5, 87  
 Gao L., Navarro J. F., Cole S., Frenk C. S., White S. D. M., Springel V., Jenkins A., Neto A. F., 2008, MNRAS, 387, 536  
 Gottloeber S., Klypin A., 2008, ArXiv e-prints  
 Jang-Condell H., Hernquist L., 2001, ApJ, 548, 68  
 Jing Y. P., 2000, ApJ, 535, 30  
 Kim J., Park C., Gott III J. R., Dubinski J., 2009, ApJ, 701, 1547  
 Klypin A., Holtzman J., 1997, ArXiv Astrophysics e-prints  
 Klypin A. A., Trujillo-Gomez S., Primack J., 2011, ApJ, 740, 102  
 Knebe A. et al., 2011, MNRAS, 415, 2293  
 Knebe A., Power C., 2008, ApJ, 678, 621  
 Kravtsov A. V., Klypin A. A., Khokhlov A. M., 1997, Rev.Astrn.Astrophys., 111, 73  
 Ludlow A. D., Navarro J. F., Angulo R. E., Boylan-Kolchin M., Springel V., Frenk C., White S. D. M., 2014, MNRAS, 441, 378  
 Ludlow A. D., Navarro J. F., Li M., Angulo R. E., Boylan-Kolchin M., Bett P. E., 2012, MNRAS, 427, 1322  
 Macciò A. V., Dutton A. A., van den Bosch F. C., 2008, MNRAS, 391, 1940  
 Macciò A. V., Dutton A. A., van den Bosch F. C., Moore B., Potter D., Stadel J., 2007, MNRAS, 378, 55  
 Meneghetti M., Rasia E., 2013, ArXiv e-prints  
 Navarro J. F., Frenk C. S., White S. D. M., 1997, ApJ, 490, 493  
 Navarro J. F. et al., 2004, MNRAS, 349, 1039  
 Neto A. F. et al., 2007, MNRAS, 381, 1450

Nuza S. E. et al., 2013, MNRAS, 432, 743  
 Power C., Knebe A., Knollmann S. R., 2012, MNRAS, 419, 1576  
 Prada F., Klypin A. A., Cuesta A. J., Betancort-Rijo J. E., Primack J., 2012, MNRAS, 423, 3018  
 Prada F., Klypin A. A., Simonneau E., Betancort-Rijo J., Patiri S., Gottlöber S., Sanchez-Conde M. A., 2006, ApJ, 645, 1001  
 Riebe K. et al., 2013, Astronomische Nachrichten, 334, 691  
 Shaw L. D., Weller J., Ostriker J. P., Bode P., 2006, ApJ, 646, 815  
 Springel V., 2005, MNRAS, 364, 1105  
 Teyssier R. et al., 2009, Astr.Astroph., 497, 335  
 Tinker J., Kravtsov A. V., Klypin A., Abazajian K., Warren M., Yepes G., Gottlöber S., Holz D. E., 2008, ApJ, 688, 709  
 Watson W. A., Iliev I. T., Diego J. M., Gottlöber S., Knebe A., Martínez-González E., Yepes G., 2013, ArXiv e-prints  
 Zhao D. H., Jing Y. P., Mo H. J., Börner G., 2009, ApJ, 707, 354  
 Zhao D. H., Mo H. J., Jing Y. P., Börner G., 2003, MNRAS, 339, 12

## APPENDIX A: PARAMETERS FOR THE CONCENTRATION - MASS RELATION

Table A1 gives parameters for approximation eq.(24) for different simulations, virial mass definitions, halo selection criteria, and redshifts.

**Table A1.** Parameters for the concentration - mass relation given by eq.(24) for Planck cosmology. Halos are defined using the overdensity 200 criterion.

Redshift	Parameter		
	$C_0$	$\gamma$	$M_0/10^{12}h^{-1}M_\odot$
Relaxed halos selected by mass			
0.00	7.75	0.100	$4.5 \times 10^5$
0.35	6.70	0.095	$2.0 \times 10^4$
0.50	6.25	0.092	$8.0 \times 10^3$
1.00	5.02	0.088	780
1.44	4.19	0.085	160
2.15	3.30	0.083	27
2.50	3.00	0.080	14
2.90	2.72	0.080	6.8
4.10	2.40	0.080	1.6
5.40	2.10	0.080	0.30
All halos selected by mass			
0.00	7.40	0.120	$5.5 \times 10^5$
0.35	6.25	0.117	$1.0 \times 10^5$
0.50	5.65	0.115	$2.0 \times 10^4$
1.00	4.30	0.110	900
1.44	3.53	0.095	300
2.15	2.70	0.085	42
2.50	2.42	0.080	17
2.90	2.20	0.080	8.5
4.10	1.92	0.080	2.0
5.40	1.65	0.080	0.3
Relaxed halos selected by $V_{\max}$			
0.00	8.0	0.100	$2.0 \times 10^5$
0.35	6.82	0.095	$9.0 \times 10^3$
0.50	6.40	0.092	$4.5 \times 10^3$
1.00	5.20	0.088	600
1.44	4.35	0.085	150
2.15	3.50	0.080	27
2.50	3.12	0.080	11
2.90	2.85	0.080	5.5
4.10	2.55	0.080	1.5
5.40	2.16	0.080	0.22
All halos selected by $V_{\max}$			
0.00	7.75	0.115	$5.5 \times 10^5$
0.35	6.50	0.115	$1.8 \times 10^4$
0.50	5.95	0.115	$6.0 \times 10^3$
1.00	4.55	0.110	600
1.44	3.68	0.105	150
2.15	2.75	0.100	20
2.50	2.50	0.095	10
2.90	2.25	0.090	5.0
4.10	2.05	0.080	1.5
5.40	1.76	0.080	0.25

**Table A2.** Parameters for the concentration - mass relation given by eq.(24) for Planck cosmology. Halos are defined using the virial overdensity criterion.

Redshift	Parameter		$M_0/10^{12}h^{-1}M_\odot$
	$c_0$	$\gamma$	
Relaxed halos selected by mass			
0.00	10.2	0.100	$1. \times 10^5$
0.35	7.85	0.095	$1.2 \times 10^4$
0.50	7.16	0.092	$5.5 \times 10^3$
1.00	5.45	0.088	700
1.44	4.55	0.085	180
2.15	3.55	0.080	30
2.50	3.24	0.080	15
2.90	2.92	0.080	7.0
4.10	2.60	0.080	1.9
5.40	2.30	0.080	0.36
All halos selected by mass			
0.00	9.75	0.110	$5.0 \times 10^5$
0.35	7.25	0.107	$2.2 \times 10^4$
0.50	6.50	0.105	$1.0 \times 10^4$
1.00	4.75	0.100	1000
1.44	3.80	0.095	210
2.15	3.00	0.085	43
2.50	2.65	0.080	18
2.90	2.42	0.080	9.0
4.10	2.10	0.080	1.9
5.40	1.86	0.080	0.42
Relaxed halos selected by $V_{\max}$			
0.00	10.7	0.110	$2.4 \times 10^4$
0.35	8.1	0.100	$5.0 \times 10^3$
0.50	7.33	0.100	$2.2 \times 10^3$
1.00	5.65	0.088	520
1.44	4.65	0.085	120
2.15	3.70	0.080	25
2.50	2.35	0.080	12
2.90	2.98	0.080	5.0
4.10	2.70	0.080	1.4
5.40	2.35	0.080	0.26
All halos selected by $V_{\max}$			
0.00	10.3	0.115	$4.8 \times 10^4$
0.35	7.6	0.115	$5.0 \times 10^3$
0.50	6.83	0.115	$2.7 \times 10^3$
1.00	4.96	0.110	390
1.44	3.96	0.105	110
2.15	3.00	0.100	18
2.50	2.73	0.095	10
2.90	2.45	0.090	5.0
4.10	2.24	0.080	1.4
5.40	2.03	0.080	0.36

**Table A3.** Parameters for the concentration - mass relation given by eq.(24) for WMAP7 cosmology. Halos are defined using the 200 overdensity criterion.

Redshift	Parameter		$M_0/10^{12}h^{-1}M_\odot$
	$c_0$	$\gamma$	
Relaxed halos selected by mass			
0.0	6.90	0.090	$5.5 \times 10^5$
0.50	5.70	0.088	6000
1.00	4.55	0.086	500
1.44	3.75	0.085	100
2.15	2.9	0.085	20
2.50	2.6	0.085	10
2.90	2.4	0.085	6.0
4.10	2.2	0.085	3.0
All halos selected by mass			
0.0	6.60	0.110	$2 \times 10^6$
0.50	5.25	0.105	$6 \times 10^4$
1.00	3.85	0.103	800
1.44	3.0	0.097	110
2.15	2.1	0.095	13
2.50	1.8	0.095	6.0
2.90	1.6	0.095	3.0
4.10	1.4	0.095	1.0
Relaxed halos selected by $V_{\max}$			
0.0	7.20	0.090	$2.0 \times 10^5$
0.50	5.90	0.088	4000
1.00	4.70	0.086	400
1.44	3.85	0.085	80
2.15	3.0	0.085	13
2.50	2.7	0.085	7.0
2.90	2.5	0.085	3.5
4.10	2.3	0.085	2.0

**Table A4.** Parameters for the concentration - mass relation given by eq.(24) for WMAP7 cosmology. Halos are defined using the virial overdensity criterion.

Redshift	Parameter		
	$c_0$	$\gamma$	$M_0/10^{12}h^{-1}M_\odot$
Relaxed halos selected by mass			
0.0	9.50	0.090	$3.0 \times 10^5$
0.50	6.75	0.088	5000
1.00	5.00	0.086	450
1.44	4.05	0.085	90
2.15	3.10	0.085	15
2.50	2.80	0.085	8.0
2.90	2.45	0.085	3.5
4.10	2.20	0.085	1.5
All halos selected by mass			
0.0	9.00	0.100	$2 \times 10^6$
0.50	6.00	0.100	$7 \times 10^3$
1.00	4.30	0.100	550
1.44	3.30	0.100	90
2.15	2.30	0.095	11
2.50	2.10	0.095	6.0
2.90	1.85	0.095	2.5
4.10	1.70	0.095	1.0
Relaxed halos selected by $V_{\max}$			
0.0	9.75	0.085	$1.3 \times 10^5$
0.50	7.02	0.085	4000
1.00	5.23	0.085	400
1.44	4.25	0.085	80
2.15	3.20	0.085	11
2.50	2.90	0.085	6.0
2.90	2.50	0.085	2.5
4.10	2.35	0.085	1.2

**Table A5.** Parameters for the concentration - mass relation given by eq.(25) for Planck cosmology. Halos are defined using the 200 critical overdensity criterion.

Redshift	Parameter	
	$b_0$	$a_0$
All halos selected by mass		
0.0	0.278	0.40
0.38	0.375	0.65
0.50	0.411	0.82
1.00	0.436	1.08
1.44	0.426	1.23
2.50	0.375	1.60
2.89	0.360	1.68
5.41	0.351	1.70
Relaxed halos selected by mass		
0.0	0.522	0.95
0.38	0.550	1.06
0.50	0.562	1.15
1.00	0.562	1.28
1.44	0.541	1.39
2.50	0.480	1.66
2.89	0.464	1.70
5.41	0.450	1.72

**Table A6.** Parameters for the concentration - mass relation given by eq.(25) for Planck cosmology. Halos are defined using the virial overdensity criterion.

Redshift	Parameter	
	$b_0$	$a_0$
All halos selected by mass		
0.0	0.567	0.75
0.38	0.541	0.90
0.50	0.529	0.97
1.00	0.496	1.12
1.44	0.474	1.28
2.50	0.421	1.52
5.50	0.393	1.62
Relaxed halos selected by mass		
0.0	0.716	0.99
0.38	0.673	1.10
0.50	0.660	1.16
1.00	0.615	1.29
1.44	0.585	1.41
2.50	0.518	1.65
5.50	0.476	1.72